Extended Powell-Sabin finite element scheme for linear elastic fracture mechanics

L. Chen[a,*], H. Bahai[a], G. Alfano[a]

[a]*Brunel University London, Department of Mechanical and Aerospace Engineering, Uxbridge UB8 3PH, UK*

Abstract

Powell-Sabin B-splines, which are based on triangles, are employed in the framework of the extended finite element method (XFEM) for fracture analysis. This avoids the necessity of remeshing in discrete fracture models and increases the solution accuracy around the crack tip. Powell-Sabin B-splines are C^1-continuous throughout the whole domain. The stresses around crack tips are captured more accurately than when using elements with a standard Lagrangian interpolation. Although Powell-Sabin B-splines do not hold the Kronecker-delta property, the Heaviside function and the tip enrichment function are confined to the cracked elements only, similar to the traditional XFEM but different from the extended isogeometric method. In addition, Powell-Sabin B-splines still hold C^1-continuous throughout cracked elements. There is no need to lower the continuity at element boundaries, to confine basis function support in cracked elements. Shifting is used to ensure compatibility with the surrounding discretisation. The sub-triangle technique is employed for the numerical integration over crack elements. The versatility and accuracy of the approach to simulate crack problems are assessed in case studies, featuring mode-I and mixed-mode crack problems.

Keywords: crack; extended Powell-Sabin method; Powell-Sabin B-splines; compatibility enforcement; numerical integration

1. Introduction

The numerical modeling of fracture problems is a technically relevant and scientifically challenging issue, and has been a focal point of attention since the early simulations in the 1960s [1, 2]. Several numerical approaches such as boundary element method [3, 4], meshless method [5, 6], Galerkin method [7, 8], extended FEM (XFEM) [9, 10], scaled boundary finite element method [11], damage method [12–14] and phase field method [15] are proposed. For the crack simulation, the XFEM holds unique advantages: no need to treat cracks as geometric discontinuities, and avoiding mesh refinement around crack tips.

The XFEM was originally introduced by Belytschko et al. [16] to model linear elastic fracture problems. Then its application has been extended to model structures with inclusions and voids [17], micro-structures[18, 19], inhomogeneous materials [20], fluid mechanics [21], hydraulic fracturing [22, 23], fatigue analysis [24], etc. Basically the XFEM inserts arbitrarily shaped discontinuity by adding an additional set of discontinuous functions with own degrees of freedom to the regular field variable. It exploits the partition of unity property of finite element basis functions. For the development of the XFEM, several basis functions are employed for the interpolation of field variables. Here we name a few for references. The initial work of the XFEM utilized the Lagrange basis function for the field variable approximation [7, 9, 25]. The Lagrange basis functions have the advantage of easy understanding and easy implementation in the analysis. In the XFEM framework, the local support and Kronecker-delta property of Lagrange basis functions are essential to confine the influence of cracks locally and to shield remaining elements from the effect of crack interfaces [26]. However, due to C^0-continuity between elements in using Lagrange bases, the stress is generally discontinuous at element boundaries and the crack tip. The accuracy in the stress predication is particularly

*Corresponding author
Email address: lin.chen@brunel.ac.uk (L. Chen)

important for the stress evaluation around the crack tip. Normally, a post-processing, such as averaging over a finite domain around crack tips, is required.

The NURBS basis functions in the isogeometric method could circumvent the stress inaccuracy issue in using Lagrange bases, and have been used in the framework of the XFEM, namely extended isogeometric method (XIGA) [27–29]. The XIGA employs the same set of basis functions for the design process and for the analysis. Due to the higher order continuity of basis functions, the stress field is continuous across elements boundaries. The enhanced continuity in the stress evaluation around the crack tip is essential for crack simulations [28]. For instance, it is important for the prediction of the crack propagation direction in free crack propagation problems. However, to confine the influence of cracks locally, C^0-lines are added in cracked elements [30]. This leads to a reduced continuous basis functions, violating the merit of the isogeometric approach (namely higher order continuity). The extended meshless method has similar property and issue as the XIGA, such as higher order continuity and wide support of basis functions in the domain [31], not illustrated here for brevity. Interesting reader could refer [32] for details.

In this contribution we employ Powell-Sabin B-splines [33] for crack modelling in the framework of extended approach, called XPSM. Powell-Sabin B-splines are based on triangles. The basis functions are C^1-continuous throughout the whole domain, leading to stresses which are smooth around the crack tip. Due to the triangle definition, the XPSM confines the effect of the crack in a local area. This is an advantage over other approaches, such as the meshless method or the isogeometric method. Generally, Powell-Sabin B-splines are not isogeometric in the strict sense that the geometry can always be captured exactly, but they share with the isogeometric method the property that they can exploit standard finite element data structures by using Bézier extraction.

We start with a review of basic properties of Powell-Sabin B-splines and boundary condition enforcement. Section 3 discusses the extended Powell-Sabin finite element (XPSM). Aspects of compatibility and integration scheme are covered as well. In Section 4, numerical examples are given which demonstrate the versatility and accuracy of the method. Finally conclusions are drawn.

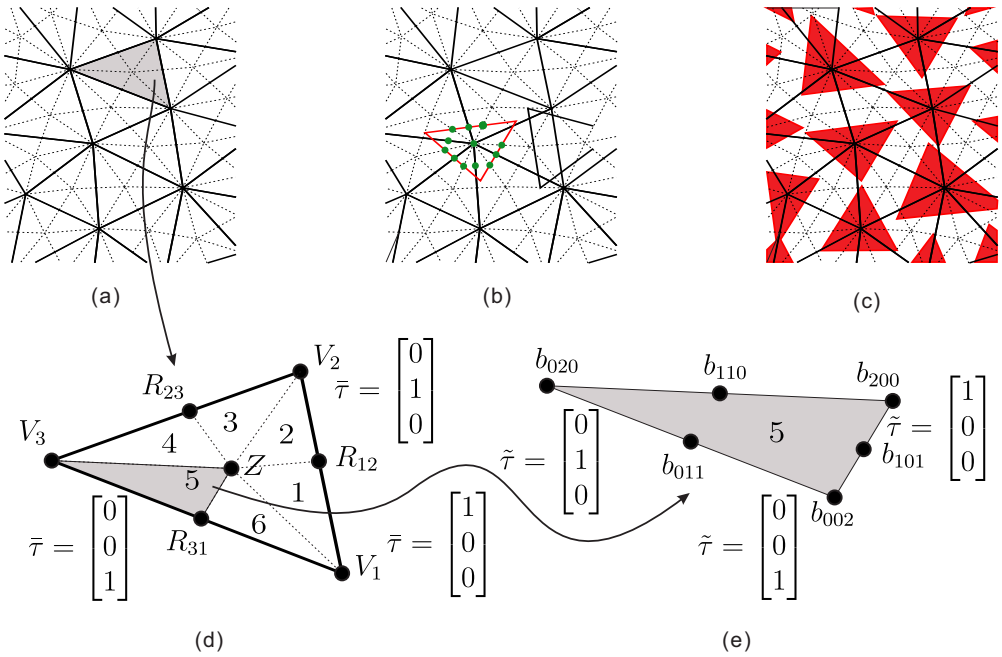

Figure 1: (a) example of a triangulation $\mathcal{T}$ (thick black lines), Powell-Sabin refinement $\mathcal{T}^*$ (thin black dashed lines) of $\mathcal{T}$; (b) Powell-Sabin triangle (red line) and relevant Powell-Sabin points (green); (c) Powell-Sabin triangles (red face) for an unstructured mesh; (d) mini-triangles of triangle e, each triangle is subdivided into six mini-triangles; (e) Barycentric coordinate system $\bar{\tau}$ of each mini-triangle.

2. Powell-Sabin finite element method

Powell-Sabin finite elements (PS-FEM) are an extension of conventional finite element methods for approximations on triangular meshes. Basis functions for the PS-FEM are C^1-continuous throughout the whole domain. In this section, we will elaborate on the concept of the PS-FEM, including basis functions, discretizations and boundary conditions. Then one could employ the PS-FEM to solve partial differential equations.

2.1. Powell-Sabin B-Splines

We consider a triangulation $\mathcal{T}$ with $e = 1, 2, \cdots, E$ triangles and N_v vertices, which is denoted by thick black lines in Figure 1(a). A vertex $\mathbf{V}_k$ of the triangulation $\mathcal{T}$ has the coordinate $\boldsymbol{\xi} = (x_1, x_2)$. m_k triangles are attached to the vertex $\mathbf{V}_k$, denoted as the molecule Ω_k. Each triangle e has a barycentric coordinate $\bar{\boldsymbol{\tau}} = (\tau_1, \tau_2, \tau_3)$, see Figure 1(d). To construct Powell-Sabin B-splines, which are C^1-continuous, each triangle e is split into six ($n = 1, 2, \cdots, 6$) mini-triangles, cf. Figure 1(d). This leads to the Powell-Sabin refinement $\mathcal{T}^*$, see Figure 1(a). Each mini-triangle n has a barycentric coordinate $\tilde{\boldsymbol{\tau}} = (\tilde{\tau}_1, \tilde{\tau}_2, \tilde{\tau}_3)$ and Bézier ordinates $b_{r,s,t}$, cf. Figure 1(e).

For each vertex k of the triangulation $\mathcal{T}$, Powell-Sabin points are given in green as the vertex itself and points lying at the centre of the edges of $\mathcal{T}^*$, see Figure 1(b). Powell-Sabin triangles, drawn in red in Figure 1(c), are then defined for each vertex k. In order to obtain positive basis functions, the Powell-Sabin triangle is required to contain all Powell-Sabin points. Herein, we employ the algorithm of [34] to find the minimum area triangle, enclosing the convex polygon defined by the Powell-Sabin points. For the Powell-Sabin triangles on the boundary, we will consider following constraints: (i) for an angle $\gamma < 180°$, two sides of the Powell-Sabin triangle must be aligned with two boundary edges, (ii) for an angle $\gamma = 180°$, one side of the Powell-Sabin triangle must be aligned with the boundary edge, see Figure 2.

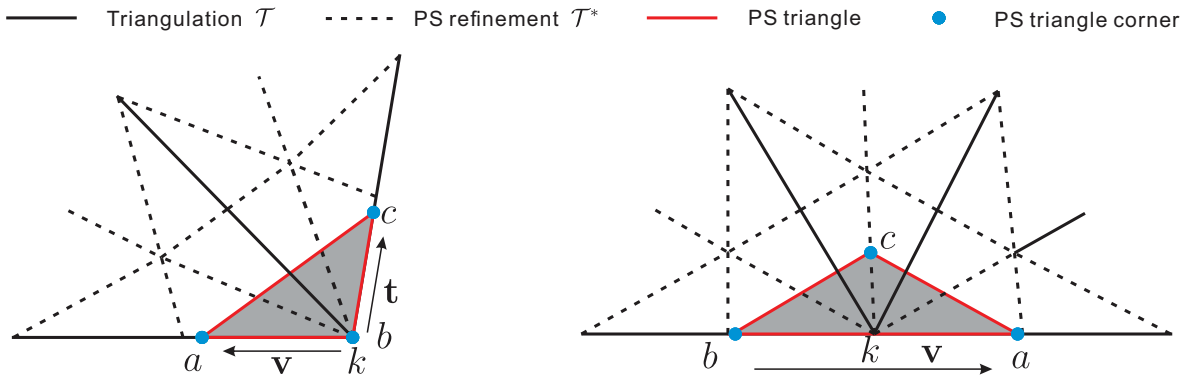

Figure 2: Strongly imposing Dirichlet boundary conditions to the corner of a Powell-Sabin triangle on boundary vertices with: an angle different from 180° (left) and equal to 180° (right).

Three Powell-Sabin B-splines N_k^j, $j = 1, 2, 3$, are defined on each vertex k with coordinate $\boldsymbol{\xi}_k = \left(x_1^k, x_2^k\right)$, i.e. one for each corner of the Powell-Sabin triangle of vertex k, and have a support in the molecule Ω_k of $\mathbf{V}_k$. Obviously, Powell-Sabin B-splines are defined by Powell-Sabin triangle corners. Thus we re-name the Powell-Sabin triangle corner as the Powell-Sabin (PS) control point, similar to the concept of control points in the isogeometric analysis. A Powell-Sabin B-spline $N_k^j(\boldsymbol{\xi})$ must be defined in each of the m_k triangles of the molecule Ω_k.

$$N_k^j(\boldsymbol{\xi}) = N_k^j\Big(\boldsymbol{\xi}(\bar{\boldsymbol{\tau}})\Big) = \sum_{e_k=1}^{m_k} N_k^{j,e_k}(\bar{\boldsymbol{\tau}}) \tag{1}$$

Each triangle in the molecule Ω_k is split into six mini-triangles, so that Powell-Sabin B-splines $N_k^{j,e_k}(\bar{\boldsymbol{\tau}})$ over a triangle e_k could be written as

$$N_k^{j,e_k}(\bar{\boldsymbol{\tau}}) = N_k^{j,e_k}\Big(\bar{\boldsymbol{\tau}}(\tilde{\boldsymbol{\tau}})\Big) = \sum_{n=1}^{6} N_{k,n}^{j,e_k}(\tilde{\boldsymbol{\tau}}) \tag{2}$$

For brevity, indices $^{e_k}_{n}$ are omitted hereafter. Powell-Sabin B-splines over each mini-triangle, $N_k^j(\tilde{\boldsymbol{\tau}})$ in Equation (2), could be formulated using Bézier ordinates $b_{r,s,t}$:

$$N_k^j(\tilde{\boldsymbol{\tau}}) = \sum_{r+s+t=2} b_{r,s,t} B_{r,s,t}^2(\tilde{\boldsymbol{\tau}}) \tag{3}$$

where $B_{r,s,t}^2(\tilde{\boldsymbol{\tau}})$ represent Bernstein polynomials:

$$B_{r,s,t}^2(\tilde{\boldsymbol{\tau}}) = \frac{2!}{r!s!t!} \tilde{\tau}_1^r \tilde{\tau}_2^s \tilde{\tau}_3^t \tag{4}$$

Bézier ordinates $b_{r,s,t}$ are obtained by first considering following properties:

$$N_k^j(\boldsymbol{V}_l) = 0 \qquad \frac{\partial}{\partial x_1} N_k^j(\boldsymbol{V}_l) = 0 \qquad \frac{\partial}{\partial x_2} N_k^j(\boldsymbol{V}_l) = 0 \tag{5}$$

for any vertex $\boldsymbol{V}_k \neq \boldsymbol{V}_l$, and we denote

$$N_k^j(\boldsymbol{V}_k) = \alpha_k^j \qquad \frac{\partial}{\partial x_1} N_k^j(\boldsymbol{V}_k) = \beta_k^j \qquad \frac{\partial}{\partial x_2} N_k^j(\boldsymbol{V}_k) = \gamma_k^j \tag{6}$$

To form a partition of unity on the domain, we must require [35]:

$$\sum_{j=1}^{3} \alpha_k^j = 1 \qquad \sum_{j=1}^{3} \beta_k^j = 0 \qquad \sum_{j=1}^{3} \gamma_k^j = 0 \tag{7}$$

and coefficients α_k^j, β_k^j and γ_k^j are subsequently obtained by solving the linear system [36]:

$$\begin{bmatrix} \alpha_k^1 & \alpha_k^2 & \alpha_k^3 \\ \beta_k^1 & \beta_k^2 & \beta_k^3 \\ \gamma_k^1 & \gamma_k^2 & \gamma_k^3 \end{bmatrix} \begin{bmatrix} x_1^{k,1} & x_2^{k,1} & 1 \\ x_1^{k,2} & x_2^{k,2} & 1 \\ x_1^{k,3} & x_2^{k,3} & 1 \end{bmatrix} = \begin{bmatrix} x_1^k & x_2^k & 1 \\ 1 & 0 & 0 \\ 0 & 1 & 0 \end{bmatrix} \tag{8}$$

in which $\boldsymbol{Q}_k^j = \left(x_1^{k,j}, x_2^{k,j}\right)$ are coordinates of Powell-Sabin triangle corners associated with each vertex k.

We next arrange Bézier ordinates $b_{r,s,t}$ in a matrix form $\boldsymbol{C}_n^e$ and denote Powell-Sabin B-splines associated with each mini-triangle n in element e by $\boldsymbol{N}_n^e$. To implement the method in existing finite element codes Bézier extraction is used [37]:

$$\boldsymbol{N}_n^e = \boldsymbol{C}_n^e \boldsymbol{B} \tag{9}$$

over each mini-triangle n in element e with six Bernstein polynomials, contained in the vector $\boldsymbol{B}$ [37]. Figure 3 gives an example of three Powell-Sabin B-splines associated with a vertex m. In the figure, the basis functions are non-zero only in the molecule Ω_m of the vertex m. Here, the molecule Ω_m contains five triangle elements surrounding the vertex m. This is similar to Lagrange bases, confining the influence of basis functions in a local manner. However, the basis functions are C^1-continuous throughout the molecule Ω_m. As illustrated in Figure 3, the basis functions are smaller than one, which indicates that Powell-Sabin B-spines do not hold the Kronecker-delta property.

2.2. *Governing equations and finite element discretization*

Assuming linear elastic material behaviour, omitting body force, the equilibrium equations read:

$$\begin{cases} \nabla \cdot \boldsymbol{\sigma} = \mathbf{0} & \text{on} \quad \Omega \\ \mathbf{u} = \hat{\mathbf{u}} & \text{on} \quad \Gamma_u \\ \boldsymbol{\sigma} \cdot \mathbf{n} = \hat{\mathbf{t}} & \text{on} \quad \Gamma_t \end{cases} \tag{10}$$

where Γ_u are essential boundaries with prescribed displacements $\hat{\mathbf{u}}$. Γ_t denote Neumann boundaries with prescribed tractions $\hat{\mathbf{t}}$. $\mathbf{n}$ denotes the normal vector at boundaries, and $\boldsymbol{\sigma}$ is the Cauchy stress tensor, which relates to $\boldsymbol{\varepsilon}$ as

$$\boldsymbol{\sigma} = \mathbf{D}\boldsymbol{\varepsilon} \qquad \boldsymbol{\varepsilon} = \frac{1}{2}\left(\nabla \mathbf{u} + (\nabla \mathbf{u})^{\mathrm{T}}\right) \qquad \text{on} \qquad \Omega \tag{11}$$

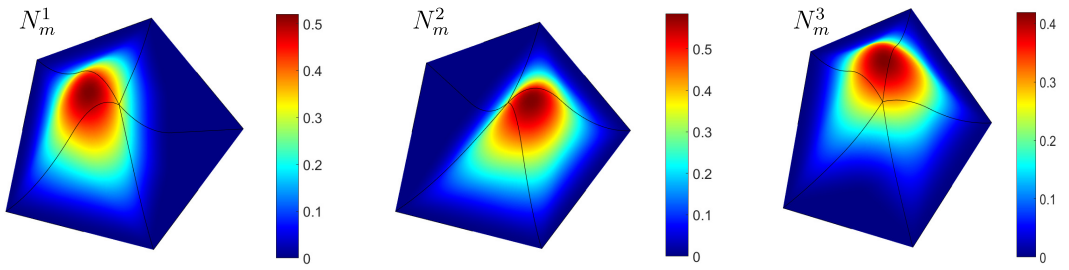

Figure 3: Example of three Powell-Sabin B-splines associated with a vertex m. In the figure, five triangle elements are attached to vertex m, bounded by thick black lines.

with $\mathbf{D}$ the fourth-order elastic stiffness tensor.

The governing unconstrained weak form of Equation (10) is given as:

$$\int_{\Omega} \delta\boldsymbol{\varepsilon} : \boldsymbol{\sigma} \mathrm{d}\Omega - \int_{\Gamma_t} \delta\mathbf{u} \cdot \hat{\mathbf{t}} \mathrm{d}\Gamma = 0 \qquad \forall \delta\mathbf{u} \in \nu_0 \tag{12}$$

where $\delta\boldsymbol{\varepsilon}$ and $\delta\mathbf{u}$ are the virtual strain and virtual displacement, respectively.

The solution $\mathbf{u}$ belongs to the function space ν:

$$\nu = \left\{ \boldsymbol{v} : v_i \in H^1(\Omega),\, v_i|\Gamma_u = \hat{u}_i \right\} \qquad \nu_0 = \left\{ \boldsymbol{v} : v_i \in H^1(\Omega),\, v_i|\Gamma_u = 0 \right\} \tag{13}$$

in which H^1 denotes the first-order Sobolev space.

To discretize Equation (12), we employ Powell-Sabin B-splines for the description of the geometry as well as for the interpolation of the displacement field:

$$\mathbf{x} = \sum_{k=1}^{N_v} \sum_{j=1}^{3} N_k^j \boldsymbol{X}_k^j = \mathbf{N}^e \mathbf{X}^e \qquad \mathbf{u} = \sum_{k=1}^{N_v} \sum_{j=1}^{3} N_k^j \boldsymbol{U}_k^j = \mathbf{N}^e \mathbf{U}^e \tag{14}$$

where $\boldsymbol{X}_k^j$ represents coordinates of Powell-Sabin triangle corners (Powell-Sabin control points) $\boldsymbol{Q}_k^j$; $\boldsymbol{U}_k^j$ denotes degrees of freedom at $\boldsymbol{Q}_k^j$ and N_v is the total number of vertices. $\mathbf{N}^e$, $\mathbf{X}^e$ and $\mathbf{U}^e$ are shape functions, coordinates and degrees of freedom (DOFs) associated with each element e.

Considering the kinematic relation, Equation (11), and the Powell-Sabin approximation, Equation (14), the weak form, Equation (12), yields a set of system equations:

$$\mathbf{K}\mathbf{U} = \mathbf{f} \tag{15}$$

where $\mathbf{K}$ denotes the stiffness matrix, $\mathbf{f}$ represents the force vector and $\mathbf{U}$ is the displacement control variable vector. $\mathbf{K}$ and $\mathbf{f}$ are assembled from the element stiffness matrix and element force vector, respectively.

$$\mathbf{K}_e = \int_{\Omega_e} \mathbf{B}_e^{\mathrm{T}} \mathbf{D} \mathbf{B}_e \mathrm{d}\Omega \qquad \mathbf{f}_e = \int_{\Gamma_t^e} \mathbf{N}_e^{\mathrm{T}} \hat{\mathbf{t}} \mathrm{d}\Gamma \tag{16}$$

in which matrices $\mathbf{N}_e$ and $\mathbf{B}_e$ contain shape functions and their derivatives associated with each element e.

2.3. Essential boundary conditions

From Equations (6) and (7), Powell-Sabin B-splines do not satisfy the Kronecker-delta property and are non-interpolatory at the vertex. Thus, imposing $\mathbf{u} = \hat{\mathbf{u}}$ on Γ_u is not as trivial as in standard finite elements. In this section, we will present implicit methods to impose essential boundary conditions.

2.3.1. Strongly imposing Dirichlet boundary condition

For problems with analytical solutions available, we could impose essential boundary conditions strongly for Powell-Sabin elements. In Section 2.1, a special choice of Powell-Sabin triangle is given along the boundary: vertex with an angle $\gamma < 180°$ (Figure 2(left)), and vertex with an angle $\gamma = 180°$ (Figure 2(right)). Equation (8) could be formulated in terms of nodal degrees of freedom U

$$\begin{bmatrix} \alpha_k^a & \alpha_k^b & \alpha_k^c \\ \beta_k^a & \beta_k^b & \beta_k^c \\ \gamma_k^a & \gamma_k^b & \gamma_k^c \end{bmatrix} \begin{bmatrix} U^{k,a} \\ U^{k,b} \\ U^{k,c} \end{bmatrix} = \begin{bmatrix} U^k \\ \frac{\partial U^k}{\partial x_1} \\ \frac{\partial U^k}{\partial x_2} \end{bmatrix}, \tag{17}$$

where $U^{k,i}$ is nodal degree of freedom of Powell-Sabin control point i ($i = a, b, c$), associated with vertex k; U^k denotes the displacement at vertex k. $\nabla U^k = \left[\frac{\partial U^k}{\partial x_1} \; \frac{\partial U^k}{\partial x_2}\right]$ is the gradient of U^k.

For the case of $\gamma < 180°$, we have following relations for coefficients α_k^i, β_k^i and γ_k^i ($i = a, b, c$):

$$\begin{aligned} &\alpha_k^a = \alpha_k^c = 0, \quad \alpha_k^b = 1, \\ &\begin{bmatrix} \beta_k^a \\ \gamma_k^a \end{bmatrix} \cdot \mathbf{t} = 0, \quad \begin{bmatrix} \beta_k^c \\ \gamma_k^c \end{bmatrix} \cdot \mathbf{v} = 0, \end{aligned} \tag{18}$$

where $\mathbf{t}$ and $\mathbf{v}$ are unit vectors along the boundary, see Figure 2(left)

$$\mathbf{t} = \frac{\mathbf{x}_a - \mathbf{x}_b}{\|\mathbf{x}_a - \mathbf{x}_b\|}, \qquad \mathbf{v} = \frac{\mathbf{x}_c - \mathbf{x}_b}{\|\mathbf{x}_c - \mathbf{x}_b\|} \tag{19}$$

From Equations (17) and (18), we have:

$$U^{k,b} = U^k, \qquad U^{k,a} = U^k + \frac{\nabla U^k \cdot \mathbf{v}}{\begin{bmatrix} \beta_k^a \\ \gamma_k^a \end{bmatrix} \cdot \mathbf{v}}, \qquad U^{k,c} = U^k + \frac{\nabla U^k \cdot \mathbf{t}}{\begin{bmatrix} \beta_k^c \\ \gamma_k^c \end{bmatrix} \cdot \mathbf{t}} \tag{20}$$

For the case of $\gamma = 180°$, coefficients α_k^i, β_k^i and γ_k^i ($i = a, b, c$) should satisfy

$$\begin{aligned} &\alpha_k^a \neq 0, \quad \alpha_k^b \neq 0, \quad \alpha_k^c = 0, \\ &\qquad\qquad\qquad \begin{bmatrix} \beta_k^c \\ \gamma_k^c \end{bmatrix} \cdot \mathbf{v} = 0, \end{aligned} \tag{21}$$

where $\mathbf{v}$ denotes the unit vector along the boundary given in Equation (19), see Figure 2(right).

Equations (17) and (21) lead to

$$U^{k,a} = \frac{U^k \Delta_1 - \alpha_k^b \nabla U^k \cdot \mathbf{v}}{\alpha_k^a \Delta_1 - \alpha_k^b \Delta}, \qquad U^{k,b} = \frac{-U^k \Delta + \alpha_k^a \nabla U^k \cdot \mathbf{v}}{\alpha_k^a \Delta_1 - \alpha_k^b \Delta}, \tag{22}$$

with $\Delta = \begin{bmatrix} \beta_k^a \\ \gamma_k^a \end{bmatrix} \cdot \mathbf{v}$, $\Delta_1 = \begin{bmatrix} \beta_k^b \\ \gamma_k^b \end{bmatrix} \cdot \mathbf{v}$.

Once obtaining $U^{k,i}$, we apply it directly in the system of equations like in the standard finite element method.

2.3.2. Lagrange multiplier method

If analytical solutions for the displacement $\mathbf{u}$ are not available, one should consider to weakly enforce essential boundary conditions. In this study, the Lagrange multiplier method is adopted for weak imposition of essential boundary conditions. This method introduces a new unknown vector $\boldsymbol{\lambda}$. We discretize Lagrange multipliers $\boldsymbol{\lambda}$ and displacement filed $\mathbf{u}$ on the essential boundary Γ_u by using Powell-Sabin B-splines:

$$\boldsymbol{\lambda} = \sum_{k=1}^{N_{bv}} \sum_{j=1}^{3} N_k^j \boldsymbol{\lambda}_k^j = \mathbf{N}_b^e \boldsymbol{\lambda}_b^e, \qquad \mathbf{u} = \sum_{k=1}^{N_{bv}} \sum_{j=1}^{3} N_k^j \mathbf{U}_k^j = \mathbf{N}_b^e \mathbf{U}_b^e, \tag{23}$$

with N_{bv} total number of vertices on the essential boundary Γ_u. $\mathbf{N}_b^e$ denotes the element boundary shape function matrix. $\boldsymbol{\lambda}_b^e$ and $\mathbf{U}_b^e$ denote degrees of freedom associated with element boundaries.

Applying the Lagrange multiplier method, the weak form Equation (12) is reformulated as

$$\int_\Omega \delta\boldsymbol{\varepsilon} : \boldsymbol{\sigma} \mathrm{d}\Omega - \int_{\Gamma_t} \delta\mathbf{u} \cdot \hat{\mathbf{t}} \mathrm{d}\Gamma - \int_{\Gamma_u} \delta\boldsymbol{\lambda} \cdot (\mathbf{u} - \hat{\mathbf{u}}) \, \mathrm{d}\Gamma - \int_{\Gamma_u} \delta\mathbf{u} \cdot \boldsymbol{\lambda} \, \mathrm{d}\Gamma = 0, \tag{24}$$

Lagrange multipliers $\boldsymbol{\lambda}$ introduce additional unknowns on the boundary Γ_u, which could be interpreted as reactive tractions, i.e. $\boldsymbol{\lambda} = \boldsymbol{\sigma}(\mathbf{u}) \cdot \mathbf{n}$ on Γ_u. Equation (24) yields following system of equations:

$$\begin{bmatrix} \mathbf{K} & \mathbf{G} \\ \mathbf{G}^T & \mathbf{0} \end{bmatrix} \begin{bmatrix} \mathbf{u}^e \\ \boldsymbol{\lambda}^e \end{bmatrix} = \begin{bmatrix} \mathbf{f} \\ \mathbf{f}_l \end{bmatrix}, \tag{25}$$

where

$$\mathbf{G} = \int_{\Gamma_u} \mathbf{N}^T \mathbf{N}_b \, \mathrm{d}\Gamma \qquad \mathbf{f}_l = \int_{\Gamma_u} \mathbf{N}_b^T \hat{\mathbf{u}} \, \mathrm{d}\Gamma, \tag{26}$$

where $\mathbf{N}$ and $\mathbf{N}_b$ are shape functions related to the element and the element boundary, respectively.

3. Extended Powell-Sabin finite element analysis

In the extended finite element method (XFEM), cracks are numerically modeled by coupling discontinuous displacement field into the finite element displacement approximation, based on the partition of unity [9]. Powell-Sabin B-splines are C^1-continuous throughout the whole domain. This is beneficial for the stress evaluation. Here, we will extend Powell-Sabin B-splines into the framework of the XFEM, called XPSM. In the XPSM, the Powell-Sabin approximation is locally enriched to simulate discontinuities and singular fields. In Equation (1), the Powell-Sabin triangle only has a support in the molecule of each vertex, confining the influence of the basis function in a local area, also see Figure 3. According to the location of cracks, only few DOFs are added to the original PS-FEM model. Thus, the XPSM holds the higher continuity of Powell-Sabin B-splines, but confines the crack in a local area. This is an advantage of PS-FEM over other approaches, such as the meshless method or the isogeometric method. To elaborate on the concept of the XPSM, we take an edge cracked square plate as an illustrative example, see Figure 4. An initial crack is placed in the middle of the plate. The plate is subjected to pure mode-I loading. Figure 4 presents the geometry and boundary conditions of the problem, while Figures 4(b) and 4(c) show the initial triangulation of the plate and associated Powell-Sabin control points.

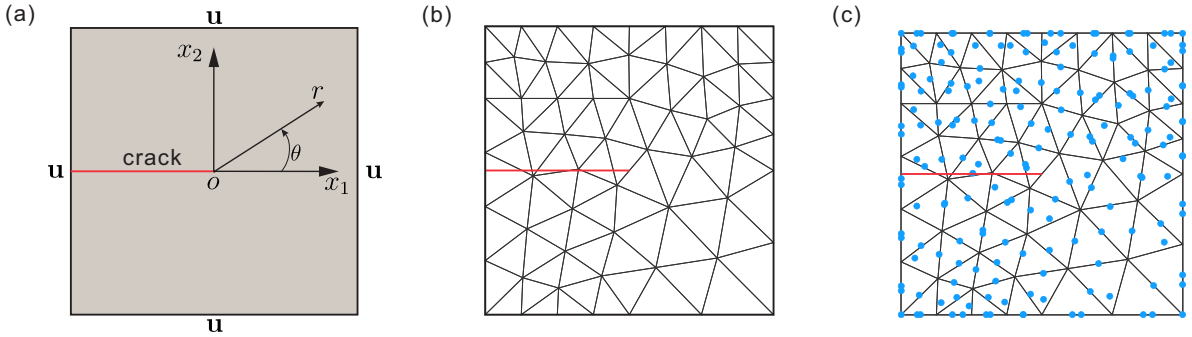

Figure 4: (a) geometry and boundary conditions for an edge cracked square plate; (b) initial triangulation; (c) Powell-Sabin control points associated with the triangulation in figure (b). In figure (b) and (c), the initial crack is introduced as the red line.

3.1. Kinematics of the displacement discontinuity

For the deformation of a cracked solid, the effect of a crack includes a jump in displacements and a singularity at the crack tip. Normally, a Heaviside function is employed to enrich Powell-Sabin control points belonging to

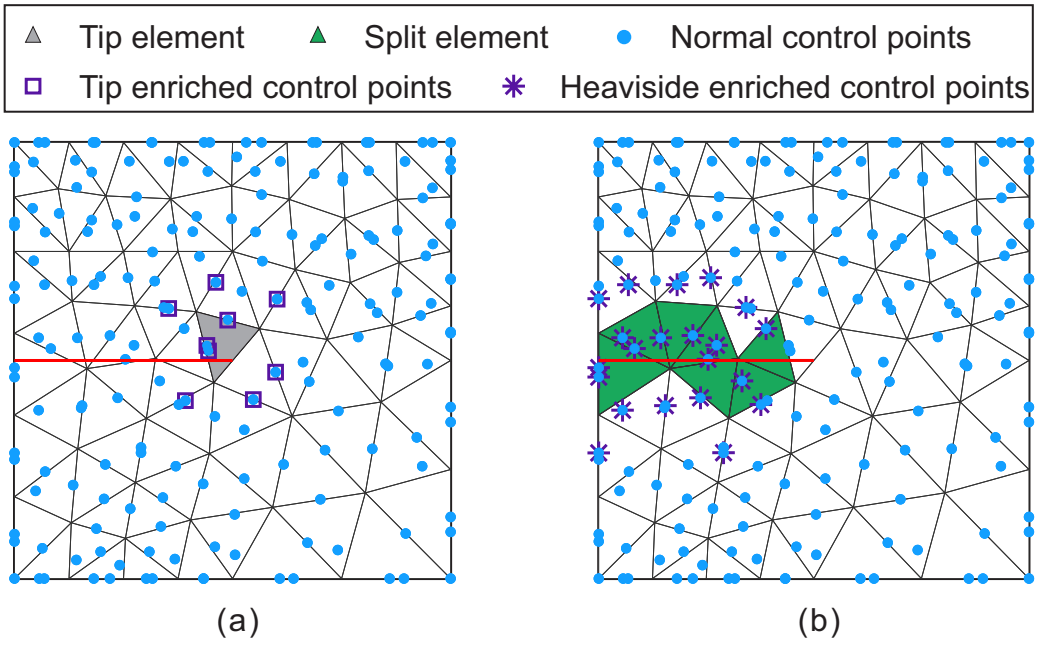

Figure 5: Various types of elements and control points. (a) element with the crack tip (tip element and tip enriched control points); (b) elements split by the crack path (split elements) and Heaviside enriched control points; in the figure, the initial crack is introduced as the red line.

the element cut by the crack path, while nodes belonging to the element containing the crack tip are enriched by asymptotic functions. Then, the approximate expression of the XPSM in the displacement field is written as

$$\mathbf{u} = \sum_{I \in \mathcal{S}} \mathbf{N}_I \mathbf{U}_I + \sum_{J \in \mathcal{S}^J} \mathbf{N}_J H(\mathbf{x}) \mathbf{d}_J + \sum_{K \in \mathcal{S}^K} \mathbf{N}_K \left(\sum_{\alpha=1}^{4} \mathbf{B}_\alpha(\mathbf{x}) \mathbf{d}_K^\alpha \right) \tag{27}$$

in which $\mathcal{S}$ is a set of normal Powell-Sabin control points for all elements; $\mathcal{S}^J$ denotes the set of enriched control points covered by elements that are split by the crack path (split elements), see Figure 5(b); $\mathcal{S}^K$ represents a set of enriched control points covered by the element with the crack tip (tip element), e.g., Figure 5(a). $\mathbf{N}_I$, $\mathbf{N}_J$ and $\mathbf{N}_K$ are Powell-Sabin B-splines with a support on corresponding elements. $\mathbf{U}_I$ denotes the DOFs associated with normal elements, while $\mathbf{d}_J$ and $\mathbf{d}_K^\alpha$ are enriched DOFs related to split elements and the tip element, respectively. If enriched control points are covered by both split elements and the tip element, the Powell-Sabin control points are preferentially enriched by the tip element enrichment scheme. In Figure 5(a), we adopt the topological enrichment scheme for the tip enrichment. Only one layer of elements in the vicinity of the crack tip is enriched [38]. To improve the accuracy of the XPSM, one could also enrich all Powell-Sabin control points within a fixed distance r_e from the crack tip, named the geometrical enrichment scheme, as illustrated in Figure 11(b). We compared the accuracy of both enrichment schemes in Section 4.1. The focus of current study is the illustration of the XPSM method, hereafter if not specified, the tip enrichment used is the topological enrichment.

$H(\mathbf{x})$ is the Heaviside function, which takes the form

$$H(\mathbf{x}) = \begin{cases} 1 & \text{if } (\mathbf{x} - \mathbf{x}^*) \cdot \mathbf{n} \geq 0 \\ -1 & \text{otherwise} \end{cases} \tag{28}$$

where $\mathbf{x}^*$ is the projection point of point $\mathbf{x}$ on the crack surface. $\mathbf{n}$ denotes the unit vector normal to the crack surface.

$\mathbf{B}_\alpha(\mathbf{x})$ represents the tip enrichment function, writing as

$$\mathbf{B}_\alpha(\mathbf{x}) = \mathbf{B}_\alpha(r, \theta) = \left[\sqrt{r} \sin\frac{\theta}{2}, \ \sqrt{r} \cos\frac{\theta}{2}, \ \sqrt{r} \sin\theta \sin\frac{\theta}{2}, \ \sqrt{r} \sin\theta \cos\frac{\theta}{2} \right] \tag{29}$$

in which $r = |\mathbf{x} - \mathbf{x}_{\text{tip}}|$ is the distance from a given point to the crack tip, and θ denotes the angle between the vector $\mathbf{x} - \mathbf{x}_{\text{tip}}$ and the tangent vector of the crack at the crack tip $\mathbf{x}_{\text{tip}}$.

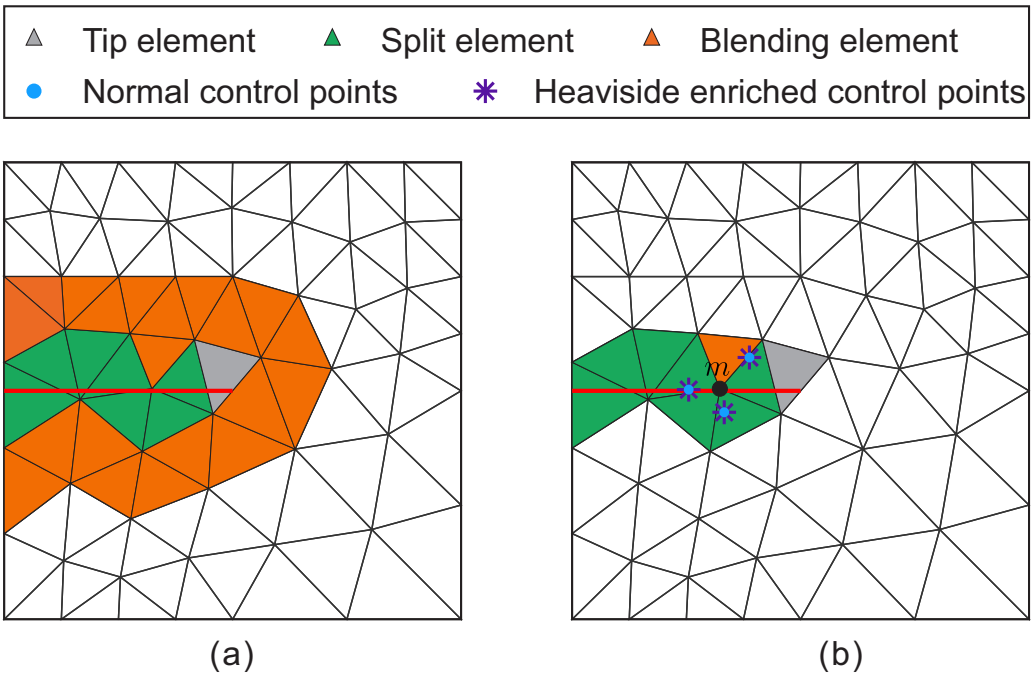

Figure 6: (a) blending elements in the XPSM; (b) blending element associated with Powell-Sabin control points of the vertex m; in the figure, the initial crack is introduced as the red line.

3.2. Compatibility enforcement

In the XPSM, elements are grouped in two parts: enriched elements and standard elements, see Figure 5. For enriched elements, all control points with support on them are enriched with DOFs, i.e., Equation (27); while for standard elements, no extra DOF is prescribed. Obviously, at the interface between enriched elements and standard ones, elements are partially enriched with extra DOFs and partially not. These elements are generally referred as blending elements, see Figure 6. In the figure, orange elements are the blending elements inter-connecting standard and enriched elements. For blending elements, the displacement field is given as

$$\mathbf{u} = \sum_{I \in \mathcal{S}} \mathbf{N}_I \mathbf{U}_I + \sum_{j=1}^{\mathcal{B}_h} \mathbf{N}_j H(\mathbf{x}) \mathbf{d}_j + \sum_{k=1}^{\mathcal{B}_t} \mathbf{N}_k \left(\sum_{\alpha=1}^{4} \mathbf{B}_\alpha(\mathbf{x}) \mathbf{d}_k^\alpha \right) \tag{30}$$

in which $\mathcal{B}_h$ and $\mathcal{B}_t$ are the set of control points enriched by Heaviside functions and tip enrichment functions, respectively. In blending elements, the partition of unity property is violated since not all control points are enriched: $\sum_{j=1}^{\mathcal{B}_h} \mathbf{N}_j \neq \mathbf{1}$ and $\sum_{k=1}^{\mathcal{B}_t} \mathbf{N}_k \neq \mathbf{1}$. Correspondingly, the completeness is not satisfied in blending elements, which yields a non-smoothness displacement field. In addition, blending elements introduce spurious terms in the displacement field, resulting in an error in the solution. In general, blending elements face a compatible issue due to the influence of partially enriched control points. Numerous contributions have been devoted on how to enforce the compatibility in blending elements [26]. Khoei have studied limitations and difficulties of the blending technique in a comprehensive manner [39]. A simple but useful approach has been presented to enforce the compatibility, namely shifting [39].

$$\mathbf{u} = \sum_{I \in \mathcal{S}} \mathbf{N}_I \mathbf{U}_I + \sum_{j=1}^{\mathcal{B}_h} \mathbf{N}_j \left(H(\mathbf{x}) - H^j \right) \mathbf{d}_j + \sum_{k=1}^{\mathcal{B}_t} \mathbf{N}_k \left(\sum_{\alpha=1}^{4} \mathbf{B}_\alpha(\mathbf{x}) \mathbf{d}_k^\alpha \right) \tag{31}$$

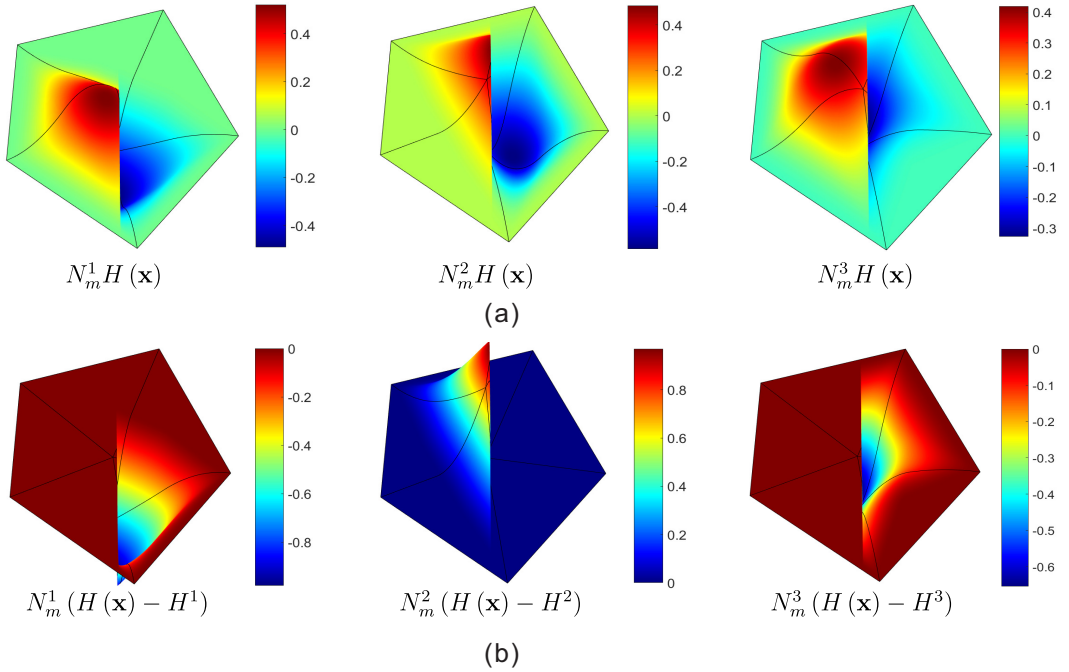

Figure 7: (a) extended Powell-Sabin basis functions of the vertex m; (b) effect of shifting on Powell-Sabin basis functions; in the figure, $H(\mathbf{x})$ is the Heaviside function; while H^i ($i = 1, 2, 3$) denotes the Heaviside value of the Powell-Sabin control point i of the vertex m.

in which H^j denotes the Heaviside value of the Powell-Sabin control point j.

Figure 7 illustrates the effect of shifting on Powell-Sabin basis functions. Figure 7(a) presents extended basis functions. Obviously, they shield an influence on blending elements. Applying shifting technique to basis functions, their influence is confined to the cracked side of elements, see Figure 7(b). Although Powell-Sabin B-splines do not hold the Kronecker-delta property, Heaviside functions are confined to cracked elements, similar to the traditional XFEM [39] but different from the extended isogeometric method [40]. In Figure 7, Powell-Sabin B-splines still hold C^1-continuous throughout cracked elements. We did not lower the continuity at element boundaries to confine basis functions in cracked elements. Generally, Powell-Sabin B-splines not only hold the property of traditional XFEM, namely confining basis functions in cracked elements, but also keep higher order continuity between elements. This is a superior aspect of the XPSM over traditional XFEM, extended isogeometric method and extended meshless method.

3.3. Numerical integration scheme

The Gauss quadrature rule is employed to integrate over XPSM elements. Due to the discontinuity in cracked elements, the accuracy of integration decreases significantly. The sub-triangle technique is employed to avoid this issue [25], see Figure 8. Due to the requirement of Powell-Sabin B-splines, each triangle in the triangulation $\mathcal{T}$ is split into six mini-triangles (Figure 8(a)). The numerical integration is performed on each mini-triangle [41]. The sub-triangulation is done on mini-triangles intersecting with the crack path, as shown in Figure 8(b). The delaunay triangulation technique is employed to subdivide the mini-triangle into sub-mini-triangles at both sides of the crack path. The command 'delaunay' of MATLAB is used here to carry out the sub-triangulation. Such sub-triangulation integration scheme is also applied to the element with the crack tip. The numerical integration over ordinary mini-triangles, not cut by the crack path, is performed normally.

The employed integration scheme is illustrated in Figure 9. For ordinary elements, not split by the crack path, only transformation T_1 and T_2 is considered in the integration. 12 Gauss points are employed in the integration for each mini-triangle. For elements with the crack path, transformation T_3 is added to transform the reference element to the parent element. The division of mini-triangles into sub-mini-triangles is performed on the parent element $\left(\hat{\xi}_1, \hat{\xi}_2\right)$. To find intersection points of the crack path and parent element edges, sign distance of mini-triangle vertexes with

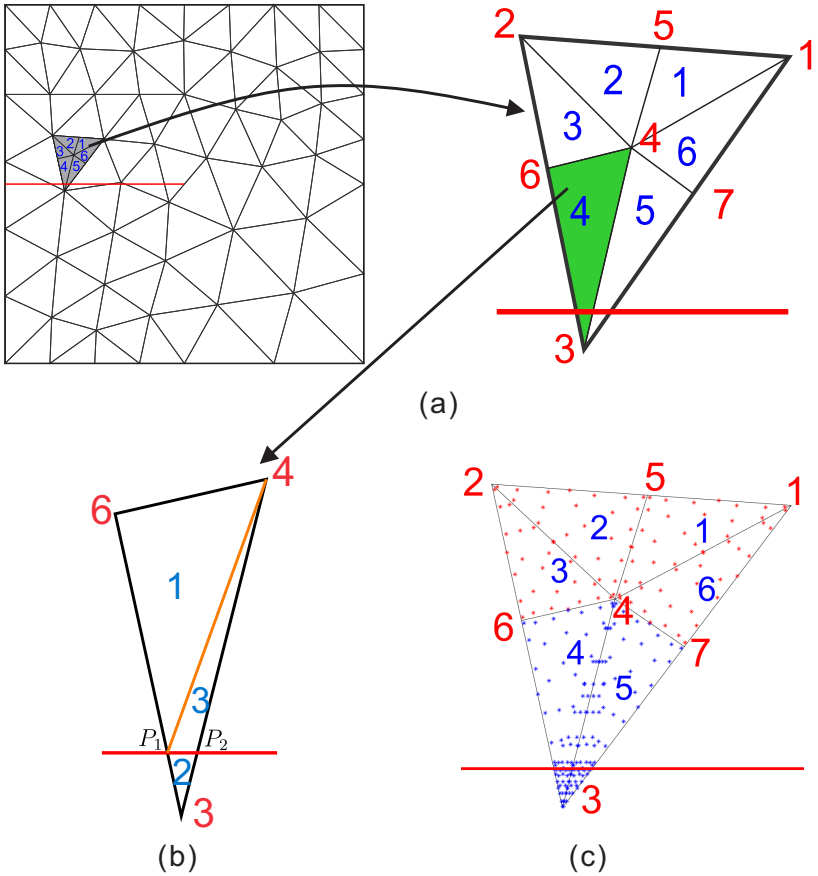

Figure 8: (a) six mini-triangles of the representative element; (b) delaunay triangulation of mini-triangle 4; (c) Gauss points in the representative element. In the figure, the initial crack is introduced as the red line. Point P_1 and P_2 are intersection points of the crack path and boundaries of mini-triangle 4. In figure (c), blue stars correspond to Gauss points in elements with the crack path, while red stars denote those without the crack path.

respect to the crack path is used. The intersection point $\hat{\xi}^{\mathrm{i}}$ is given as

$$\begin{aligned}
\hat{\xi}_1^{\mathrm{i}} &= \left(1 - \frac{D_{\mathrm{s}}^1}{D_{\mathrm{s}}^1 - D_{\mathrm{s}}^2}\right) \cdot \hat{\xi}_1^1 + \frac{D_{\mathrm{s}}^1}{D_{\mathrm{s}}^1 - D_{\mathrm{s}}^2} \cdot \hat{\xi}_1^2 \qquad \text{if} \quad D_{\mathrm{s}}^1 \cdot D_{\mathrm{s}}^2 < 0 \\
\hat{\xi}_2^{\mathrm{i}} &= \left(1 - \frac{D_{\mathrm{s}}^1}{D_{\mathrm{s}}^1 - D_{\mathrm{s}}^2}\right) \cdot \hat{\xi}_2^1 + \frac{D_{\mathrm{s}}^1}{D_{\mathrm{s}}^1 - D_{\mathrm{s}}^2} \cdot \hat{\xi}_2^2 \qquad \text{if} \quad D_{\mathrm{s}}^1 \cdot D_{\mathrm{s}}^2 < 0
\end{aligned} \tag{32}$$

in which D_{s}^1 and D_{s}^2 are the sign distance of mini-triangle vertex '1' and '2' in the physical space, respectively; while $\left(\hat{\xi}_1^1, \hat{\xi}_2^1\right)$ and $\left(\hat{\xi}_1^2, \hat{\xi}_2^2\right)$ are corresponding coordinates in the parent element $\left(\hat{\xi}_1, \hat{\xi}_2\right)$.

For the numerical integration in the element with the crack tip, we firstly find the intersection point P_1 of the crack path and the mini-triangle edge. Then we connect point P_1 and the crack tip P_c into a straight line P_1P_c, and extend the line to get the intersection point P_2 of the line and the mini-triangle edge in the physical space. This could be easily done because of only linear algebra involved. We apply the sub-triangulation on the mini-triangle intersecting with the line $P_1P_cP_2$. In current study, for elements with the crack path, 25 Gauss points are used in the integration for each min-triangle and sub-mini-triangle. In Section 4.3, we present an example of numerical integration in the element with a crack tip, see Figure 21.

The corresponding coordinate of the crack tip in the parent element is obtained similarly by applying Equation (32). We connect any mini-triangle vertex P_v and the crack tip P_c into a straight line P_vP_c. Computing the sign distance of the intersection point P_1 and P_2 with respect to the line P_vP_c and applying Equation (32) to get crack

tip coordinates in the parent element $\left(\hat{\xi}_1, \hat{\xi}_2\right)$. Even Powell-Sabin B-splines hold C^1-continuous throughout the whole domain, here we get crack tip coordinates in an analytical way, different from the isogeometric method, which requires to solve a nonlinear algebraic equation due to the higher continuity of basis functions.

Transformation T_1 and T_2 are standard in the Powell-Sabin FEM [41]. The transformation T_3 is defined as

$$\begin{aligned}\hat{\xi}_1 &= \frac{1-\bar{\xi}_1-\bar{\xi}_2}{2}\cdot\hat{\xi}_1^1+\bar{\xi}_1\cdot\hat{\xi}_1^2+\bar{\xi}_2\cdot\hat{\xi}_1^3\\ \hat{\xi}_2 &= \frac{1-\bar{\xi}_1-\bar{\xi}_2}{2}\cdot\hat{\xi}_2^1+\bar{\xi}_1\cdot\hat{\xi}_2^2+\bar{\xi}_2\cdot\hat{\xi}_2^3\end{aligned} \tag{33}$$

where $\left(\bar{\xi}_1, \bar{\xi}_2\right)$ are coordinates in the reference element, see Figure 9(a). $\left(\hat{\xi}_1^i, \hat{\xi}_2^i\right)$ $(i = 1, 2, 3)$ are coordinates of vertexes of the sub-mini-triangle '1' in Figure 9(b).

Obviously, the sub-triangulation technique employed here is reliable, considering that the crack path is straight in the parameter space and in the parent element. All numerical examples provided in current study are assumed to be straight cracks (or crack segments) in both physical and parameter spaces.

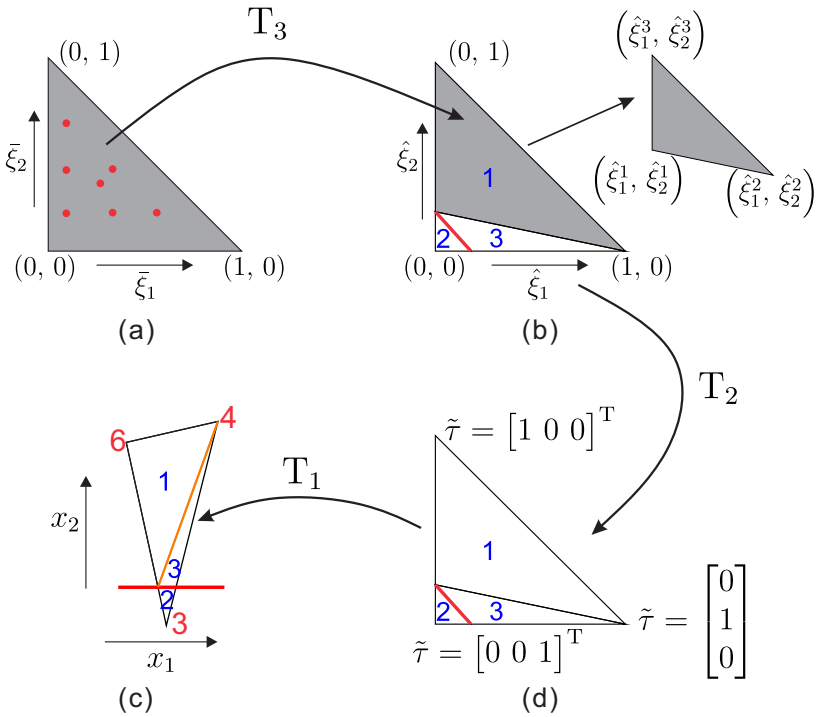

Figure 9: Transformations for numerical integration of mini-triangle 4 in Figure 8. (a) Gauss points in the reference element with coordinates $\left(\bar{\xi}_1, \bar{\xi}_2\right)$; (b) transformation T_3 from coordinates $\left(\bar{\xi}_1, \bar{\xi}_2\right)$ to the parent element $\left(\hat{\xi}_1, \hat{\xi}_2\right)$; (c) transformation T_2 from the parent element $\left(\hat{\xi}_1, \hat{\xi}_2\right)$ to barycentric coordinates $\tilde{\tau} = (\tilde{\tau}_1, \tilde{\tau}_2, \tilde{\tau}_3)$; (d) transformation T_1 from barycentric coordinates $\tilde{\tau} = (\tilde{\tau}_1, \tilde{\tau}_2, \tilde{\tau}_3)$ to the physical space (x_1, x_2). In the figure, the initial crack is introduced as the red line.

3.4. Stress intensity factors (SIFs)

The stress intensity factors are the quantitative parameters, reflecting the strength of elastic stress field at the crack tip. The concept of J-integral is employed to evaluate the energy release rate for a crack. For general mixed-mode problems, the energy release rate G can be given as the composition of stress intensity factors (SIFs)[9]

$$J = G = \frac{K_{\mathrm{I}}^2}{E^*} + \frac{K_{\mathrm{II}}^2}{E^*} \tag{34}$$

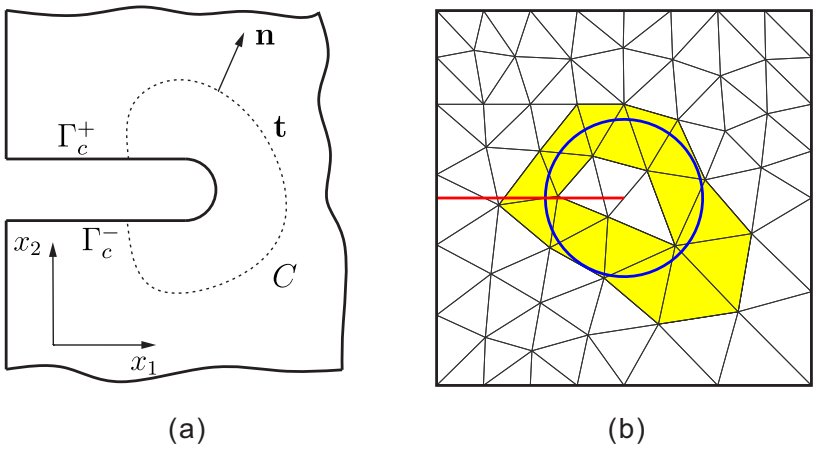

Figure 10: (a) J-integral around a notch in two dimensions; (b) triangles (yellow) chosen about the crack tip for the interaction integral. In the figure, the initial crack is introduced as the red line. The set of yellow triangles are selected as the collection of elements with a domain radius r_d about the crack tip. In current study, r_d is taken to be twice of smallest triangle element size.

in which K_{I} and K_{II} are stress intensity factors of mode-I and mode-II. E^* is a fracture parameter, relying on Young's modulus E and Poisson's ratio ν, $E^* = E$ for plane stress and $E^* = E/\left(1-\nu^2\right)$ for plane strain condition.

Theoretically, the J-integral is calculated as a contour integral along any line C in Figure 10(a) [9]. Once the J-integral obtained, we could get the SIFs. However, the contour integral is not well suitable for finite element calculation [9]. Thus in practice the SIFs are computed by the interaction integral technique. For the crack model employed in the interaction integral, two states are considered: actual state $\left(\sigma_{ij}^{(1)},\, \varepsilon_{ij}^{(1)},\, u_i^{(1)}\right)$ and auxiliary state $\left(\sigma_{ij}^{(2)},\, \varepsilon_{ij}^{(2)},\, u_i^{(2)}\right)$. The auxiliary state is chosen as asymptotic fields for mode-I and mode-II. The interaction integral takes the form [9]

$$I^{(1,2)} = \int_A \left[\sigma_{ij}^{(1)} \frac{\partial u_i^{(2)}}{\partial x_1} + \sigma_{ij}^{(2)} \frac{\partial u_i^{(1)}}{\partial x_1} - W^{(1,2)}\delta_{1j}\right] \frac{\partial q}{\partial x_j} \mathrm{d}A \tag{35}$$

with $W^{(1,2)}$ being interaction strain energy, $W^{(1,2)} = \left(\sigma_{ij}^{(1)}\varepsilon_{ij}^{(2)} + \sigma_{ij}^{(2)}\varepsilon_{ij}^{(1)}\right)/2$. q is the weight function value varying from 0 to 1. In the integral, the domain A is the collection of triangles about the crack tip, see Figure 10(b). In current study, for convenience, we consider triangles, instead of mini-triangles, to form the integration domain A in Equation (35). In the implementation, we choose triangles touched by the crack tip with a characteristic length r_d, as shown in Figure 10(b).

Once obtaining the interaction integral $I^{(1,2)}$, we could approach the SIFs by [9]

$$I^{(1,2)} = \frac{2\left(K_{\mathrm{I}}^{(1)}K_{\mathrm{I}}^{(2)} + K_{\mathrm{II}}^{(1)}K_{\mathrm{II}}^{(2)}\right)}{E^*} \tag{36}$$

Choosing separately the auxiliary state for mode-I and mode-II, the SIFs could be obtained

$$\begin{aligned} K_{\mathrm{I}} = K_{\mathrm{I}}^{(1)} &= \frac{E^*}{2} I^{(1,\text{mode-I})} \qquad \text{mode-I:} \quad K_{\mathrm{I}}^{(2)} = 1, \quad K_{\mathrm{II}}^{(2)} = 0 \\ K_{\mathrm{II}} = K_{\mathrm{II}}^{(1)} &= \frac{E^*}{2} I^{(1,\text{mode-II})} \qquad \text{mode-II:} \quad K_{\mathrm{I}}^{(2)} = 0, \quad K_{\mathrm{II}}^{(2)} = 1 \end{aligned} \tag{37}$$

For the crack propagation modelling, the propagation direction is a key factor to guild the crack growth. Here, we take the maximum circumferential stress criterion to determine the crack growth angle θ_{c} [42]

$$\theta_{\mathrm{c}} = 2\arctan\left[\frac{-2\left(\frac{K_{\mathrm{II}}}{K_{\mathrm{I}}}\right)}{1+\sqrt{1+8\left(\frac{K_{\mathrm{II}}}{K_{\mathrm{I}}}\right)^2}}\right] \tag{38}$$

once obtaining the crack growth direction θ_{c}, we could get the updated crack path with a crack increment. Here, a constant crack incremental length da is used in the study.

4. Numerical examples

To investigate the performance of the approach, we present four examples: a square plate with an edge crack, an inclined crack, a curved crack and a plate with two propagating cracks. For the square plate with an edge crack in Figure 4, analytical solutions are available in the literature [43]. The performance of the approach is assessed using the energy error norm. The error of each element is given as:

$$\|\mathbf{u}-\bar{\mathbf{u}}\|_{\mathrm{E}(\Omega_e)} = \sqrt{\left(\int_{\Omega_e} (\boldsymbol{\varepsilon}-\bar{\boldsymbol{\varepsilon}})^{\mathrm{T}} \cdot (\boldsymbol{\sigma}-\bar{\boldsymbol{\sigma}})\, \mathrm{d}\Omega\right)} \tag{39}$$

where $\mathbf{u}$, $\boldsymbol{\varepsilon}$ and $\boldsymbol{\sigma}$ stand for the analytical solution, $\bar{\mathbf{u}}$, $\bar{\boldsymbol{\varepsilon}}$ and $\bar{\boldsymbol{\sigma}}$ denote the approximate solution.The domain error is obtained by summing up the element error:

$$\|\mathbf{u}-\bar{\mathbf{u}}\|_{\mathrm{E}(\Omega)} = \sqrt{\sum\nolimits_e \left(\|\mathbf{u}-\bar{\mathbf{u}}\|_{\mathrm{E}(\Omega_e)}\right)^2} \tag{40}$$

4.1. Edge crack under far field uniform tensile loading

A square plate of the dimension 1×1 is considered with an edge crack, shown in Figure 4. The length of the initial crack is $a = 0.5$. We set Young's modulus $E = 1000$ and Poisson's ratio $\nu = 0.3$. Plane-stress conditions are assumed. Figure 4(a) shows the geometry and boundary conditions. Here we consider the displacement on the boundary corresponding to the singular stress field (parameterized by the stress intensity factor $\mathrm{K_I}$) around the initial crack tip. The analytical expressions of displacement field are given in the Appendix A. Due to available analytical solutions, imposing Dirichlet boundary condition could be performed by the formulations presented in Section 2.3.1. Figure 4(b) and (c) show an example of the triangulation and Powell-Sabin control points. Figure 5 shows enriched control points associated with cracked elements for the triangulation given in Figure 4(b).

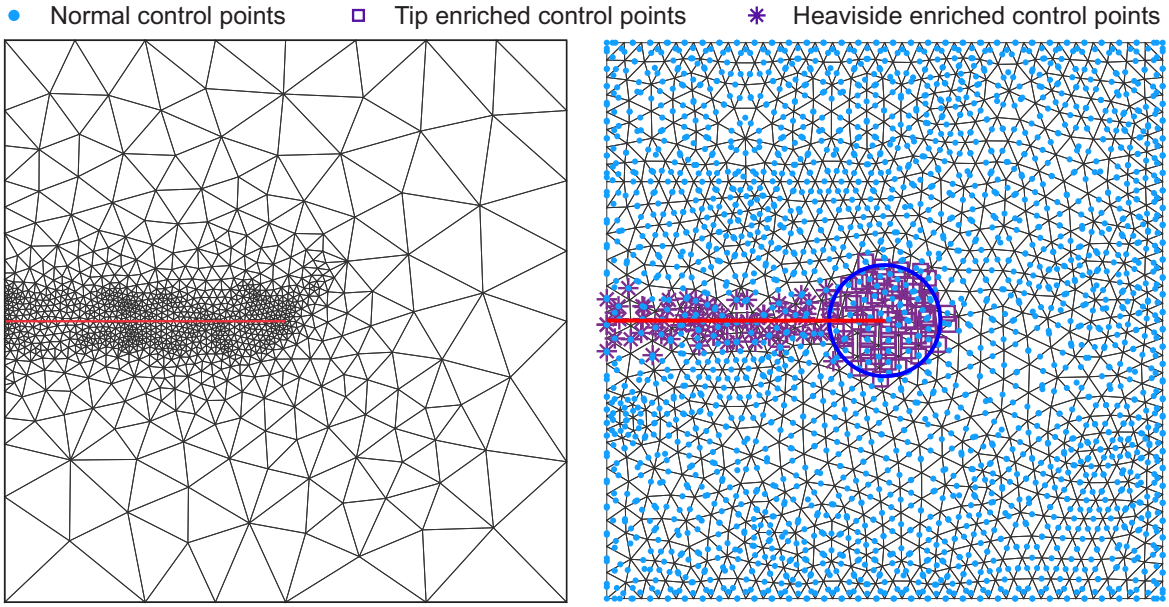

(a) local mesh refinement (b) geometrical enrichment

Figure 11: Example of local mesh refinement along the crack path and geometrical enrichment around the crack tip. In figure (b), we enrich all control points belonging to triangle vertexes located within a given distance ($r_e = 0.1$) to the crack tip.

In the analysis, we employ the mesh refinement scheme proposed by Funken et al. [44] and Geuzaine et al. [45] to locally refine the mesh around the crack path, see Figure 11(a). For brevity, the marked element for refinement is determined as follows: it starts at the crack path, and then a radial marching is done until three elements have

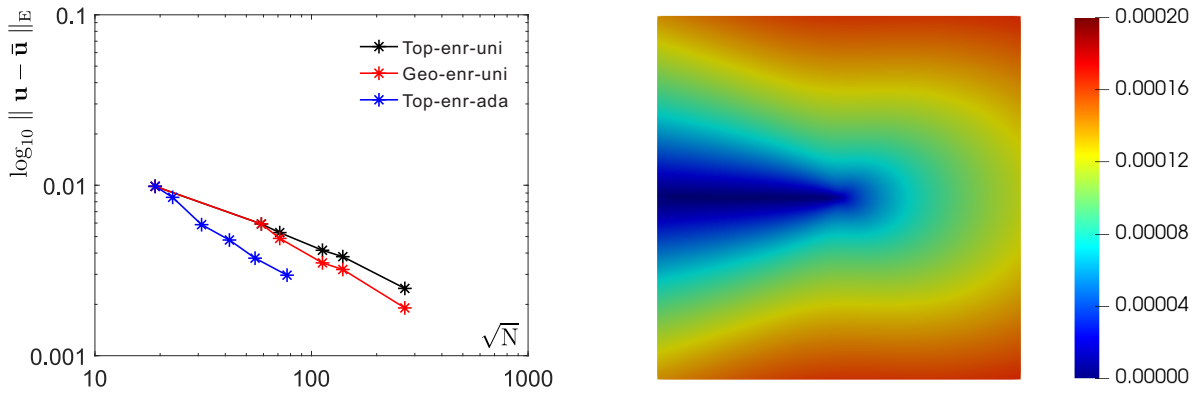

(a) energy error norm (b) contours of displacement u_1

Figure 12: Energy error norm for various number of degree of freedoms (dofs $\sqrt{N}$ scale) and contours of displacement u_1. In the figure, 'Top-enr-uni' and 'Top-enr-ada' denote separately the results from uniform and adaptive local refinement with topological tip enrichment scheme, while 'Geo-enr-uni' represents the results from uniform mesh refinement with geometrical tip enrichment scheme.

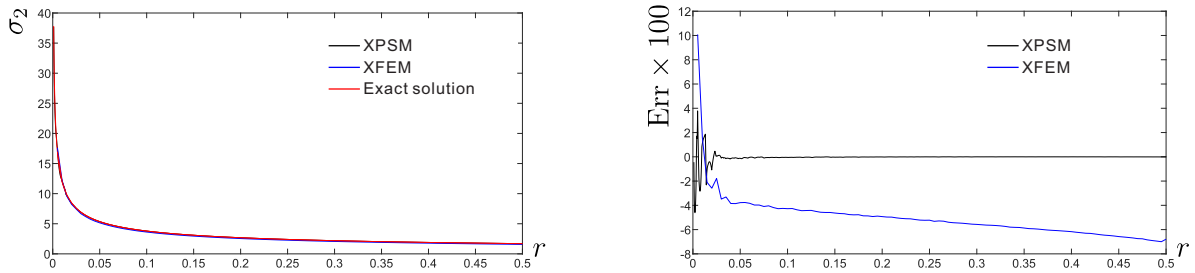

(a) σ_2 along x_1-axis (b) error of σ_2 along x_1-axis

Figure 13: σ_2 and its error along x_1-axis. In the figure, 'XFEM' stands for the results from the extended finite element method using Lagrange basis functions. r is the radius of the point with respect to the crack tip; Err is the error of the numerical solution, Err $= \frac{\sigma_2^{\text{num}} - \sigma_2^{\text{ext}}}{\sigma_2^{\text{ext}}}$, where 'num' denotes numerical results from the XPSM and XFEM, 'ext' represents the exact solution.

been crossed in all directions, see Figure 11(a). Of course, one could employ the posteriori error estimator to mark elements for refinement [46, 47]. However, it is not the focus of current study, we will work on this in the next step. In addition, to improve the accuracy of the proposed method, we also employ the geometrical enrichment scheme for the tip enrichment, see Figure 11(b).

As demonstrated in Figure 12(a), increasing the number of control points, namely decreasing the element size, improves the solution accuracy. In addition, the local refinement and geometrical tip enrichment could increase the rate of convergence, due to a smoothed gradient around the crack tip [37]. Figure 12(b) shows the contour plot of the displacement u_1 of the proposed method. Figure 13 compares the stress σ_2 obtained from the proposed method (XPSM) and extended finite element method (XFEM). In the XFEM, Lagrange basis functions are employed to approximate the displacement field. However, due to C^0-continuity between elements in using Lagrange bases, the stress σ_2 is discontinuous at element boundaries. Extra effort is needed to smooth the stress field in the domain. Here we use the commercial software Abaqus to get the stress σ_2. In Abaqus, averaging concept is employed to smooth the stress σ_2. In Figure 13(a), both the XPSM and XFEM compare well with the exact solution. Figure 13(b) presents the error of both methods. Obviously, the error of the XPSM is mainly at the crack tip due to the singularity, while that of the XFEM is throughout the whole area. In addition, the maximum error of the XPSM is around 4%, while that of the XFEM is around 10%. The improved accuracy is due to the improved continuity of Powell-Sabin B-splines.

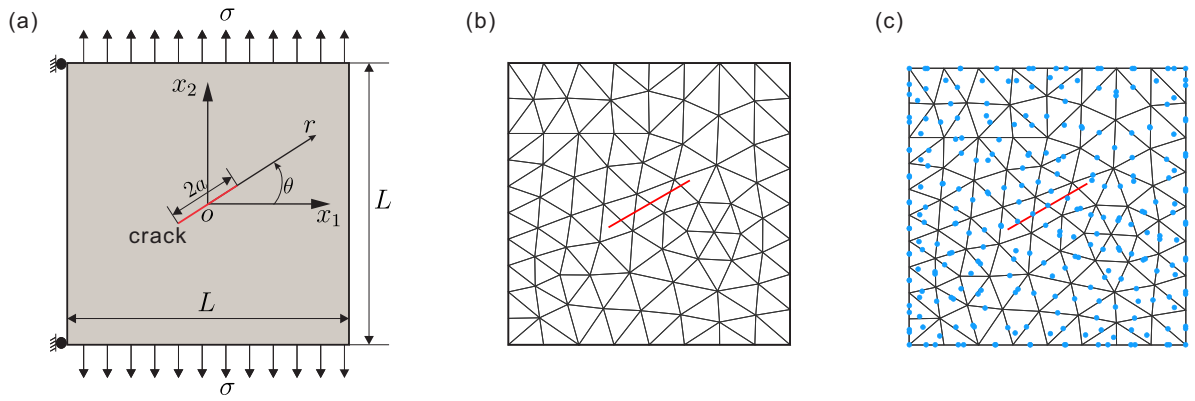

Figure 14: (a) geometry and boundary conditions for an inclined center crack problem; (b) initial triangulation; (c) Powell-Sabin control points associated with the triangulation in figure (b). In figure (b) and (c), the initial crack is introduced as the red line.

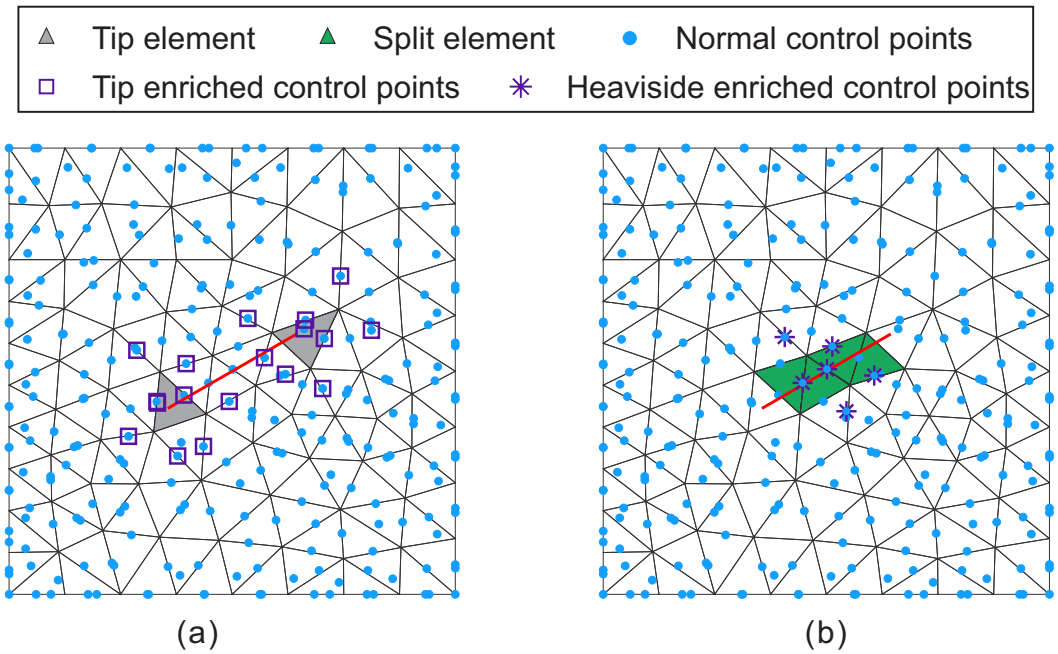

Figure 15: Various types of elements and control points for the inclined crack problem. (a) element with the crack tip (tip element and tip enriched control points); (b) elements split by the crack path (split elements) and Heaviside enriched control points; in the figure, the initial crack is introduced as the red line.

4.2. Inclined center crack in a square plate under uniaxial tension

To verify the accuracy of the present approach in the case of mixed-mode crack problems, a square plate of the dimension $L \times L = 3 \times 3$ is considered, see Figure 14. An inclined center crack is placed inside the plate, with a length $2a = 1$. The tilt angle of the crack $\theta = \pi/6$ is chosen as the demonstrative case, see Figure 14. The material parameters are $E = 1000$ and $\nu = 0.3$. Plain-strain condition is assumed. Figure 14(a) presents the geometry and boundary conditions. The uniaxial stress $\sigma = 1$ is uniformly prescribed along top and bottom edges. For known loadings σ, the exact mixed-mode stress intensity factors are given as[29]

$$\mathrm{K_I} = \sigma\sqrt{\pi a \sec\left(\frac{\pi a}{L}\right)}\cos^2\theta \qquad \mathrm{K_{II}} = \sigma\sqrt{\pi a \sec\left(\frac{\pi a}{L}\right)}\cos\theta\sin\theta \tag{41}$$

Figure 14 shows the initial triangulation and corresponding Powell-Sabin control points for the case of $\theta = \pi/6$.

Figure 15 shows enriched control points associated with cracked elements for the triangulation in Figure 14(b). In the figure, two groups of control points are enriched by the tip enrichment due to two crack tips. For each crack tip, nine control points are enriched because of three vertexes of the cracked element. The contours of maximum principal stress σ_{m} are shown in Figure 16. The stress plot of the XFEM is used to provide the reference solution, obtained from Abaqus. The figure shows that the results of the proposed method are in a good agreement with the reference solution. The stress profile presents obvious sliding between crack interfaces. The principal stress σ_{m} is close to zero on the crack surface, but the largest stress appears at the crack tip due to the stress singularity.

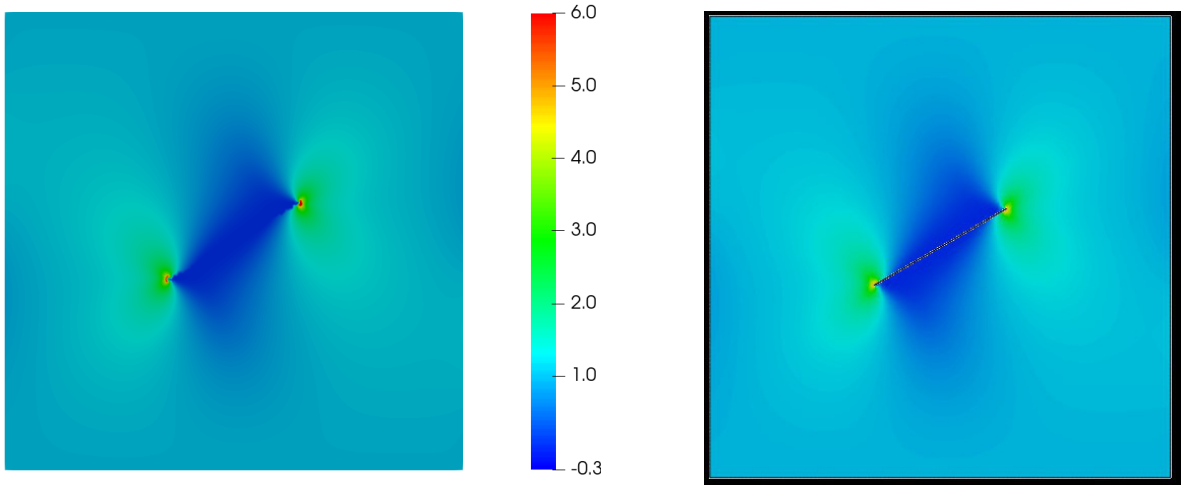

(a) contour plot of the XPSM (b) contour plot of the XFEM

Figure 16: Contour plot of maximum principal stress σ_{m}.

Figure 17 presents the SIFs of mode-I and mode-II at different inclination angle θ. The SIFs of the proposed method and XFEM agree well with the exact solution. The mode-I SIFs decrease drably with the rise of θ. The mode-II SIFs increase monotonically in $\theta \in [0, \pi/4]$, while decrease monotonically in $\theta \in [\pi/4, \pi/2]$. The mode-II SIFs attain its maximum at $\theta = \pi/4$.

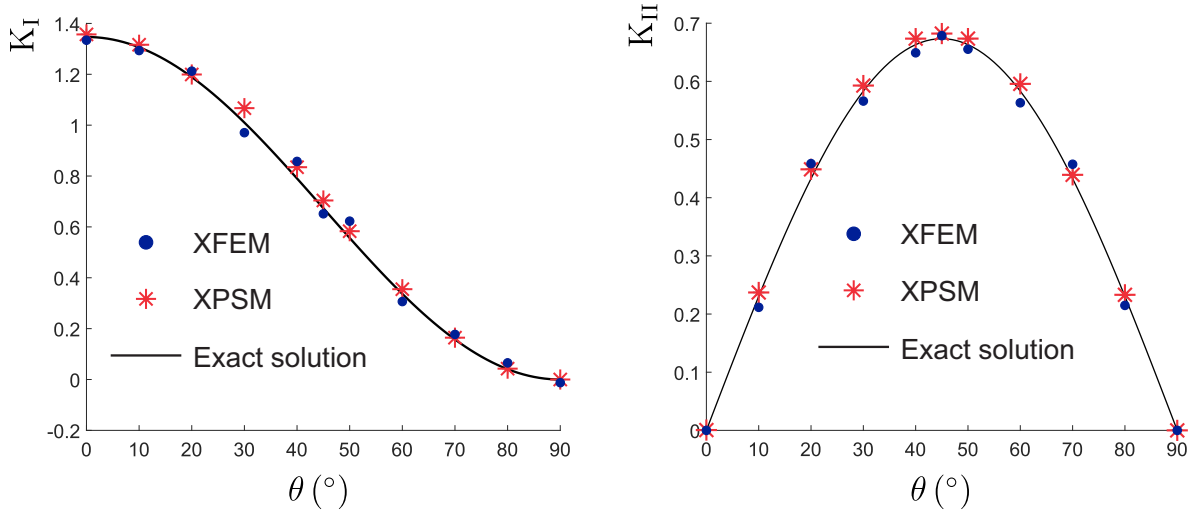

(a) mode-I SIF $\mathrm{K_I}$ (b) mode-II SIF $\mathrm{K_{II}}$

Figure 17: SIFs with different inclination angle θ for the inclined center crack problem.

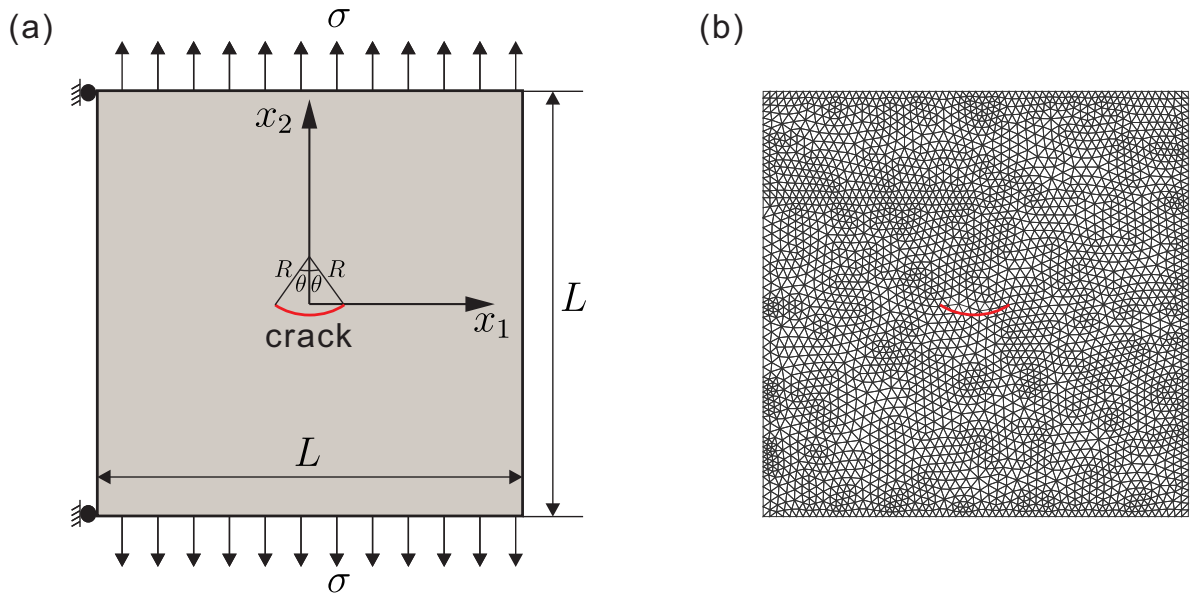

Figure 18: (a) geometry and boundary conditions for a curved center crack problem; (b) initial triangulation. In figure (b), the initial crack is introduced as the curve.

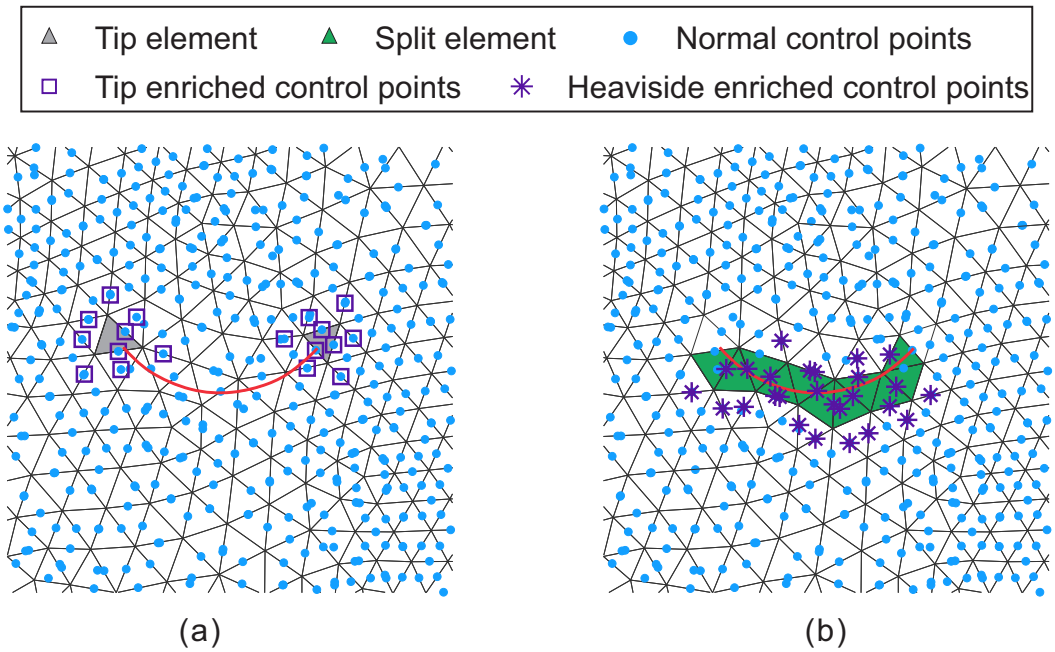

Figure 19: Various types of elements and control points for the curved crack problem. (a) elements with crack tips (tip element and tip enriched control points); (b) elements split by the crack path (split elements) and Heaviside enriched control points; in the figure, the initial crack is introduced as the red curve.

4.3. Curved crack under uniaxial tension

The mixed mode SIFs for a curved crack under uniaxial loadings is considered here. Figure 18(a) presents the geometry and boundary conditions. The uniaxial stress $\sigma = 1$ is uniformly prescribed along the top and bottom edges. The plate is in a plane strain state, with the dimension $L \times L = 40 \times 40$. The material properties of the plate are: Young's modulus $E = 1000$ and Poisson's ratio $\nu = 0.3$. An arc crack, starting at $(-2, 0)$ and ending at $(2, 0)$, is

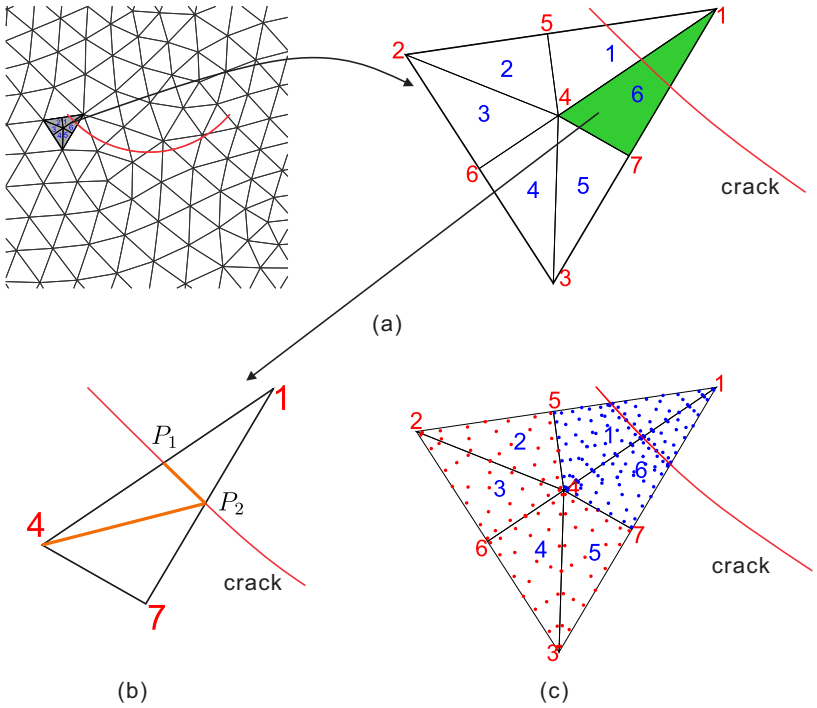

Figure 20: (a) six mini-triangles of the representative element; (b) delaunay triangulation of mini-triangle 6; (c) Gauss points in the representative element. In the figure, the initial crack is introduced as the red curve. In figure (c), point P_1 and P_2 are intersection points of the crack path and boundaries of mini-triangle 6. In figure (c), blue stars correspond to Gauss points in elements with the crack path, while red stars denote those without the crack path.

prescribed in the center of the plate. The arc angle is 2θ and the radius of the arc is R. For a central curved crack in an infinite plate, the SIFs are given as [48]

$$\mathrm{K_I} = \frac{\sigma}{2}\sqrt{\pi R \sin\theta}\left(K\cos\frac{\theta}{2} + \cos\frac{3\theta}{2}\right) \qquad \mathrm{K_{II}} = \frac{\sigma}{2}\sqrt{\pi R \sin\theta}\left(K\sin\frac{\theta}{2} + \sin\frac{3\theta}{2}\right) \tag{42}$$

with $K = \left(1 - \sin^2\theta\cos^2\theta\right) / \left(1 + \sin^2\frac{\theta}{2}\right)$. To numerically approach the analytical solution, the ratio of the model width to the crack length should be larger than 10.

For displacement boundary conditions, the bottom left corner is fixed in both directions, while the top left corner is free in the vertical direction. Here, we take the case of half crack arc angle $\theta = \pi/6$ as the demonstrative case, see Figure 18. The enriched control points are illustrated in Figure 19. For the crack tips, two groups of tip enrichment are given in Figure 19(a). For the Heaviside enrichment, we enrich elements touching the crack path.

We perform the numerical integration in cracked elements using the algorithm in Section 3.3, see Figure 20. In the figure(b), the mini-triangle '6' is cut by the crack path. We first find intersection points P_1 and P_2 of the arc and the min-triangle edge in the physical space. We connect P_1 and P_2 to get the linear line P_1P_2. Then we employ the delaunay triangulation technique to subdivide the mini-triangle into sub-mini-triangles at both sides of P_1P_2. Finally we perform the numerical integration as the scheme proposed in Figure 9. The corresponding Gauss integration points are shown in Figure 20(c).

For the numerical integration in elements with the crack tip, we first find the intersection point of the curve crack and the mini-triangle edge, e.g., point P_1 in Figure 21(b). In the figure, P_c is the crack tip. We connect P_c and P_1 to form the linear line P_1P_c. Then we extend P_1P_c in the physical space and get the intersection point P_2 of the extended line P_1P_c and the mini-triangle edge. We perform the delaunay triangulation to subdivide the mini-triangle into sub-mini-triangles at both sides of line $P_1P_cP_2$, see Figure 21(b). The numerical integration is done as the algorithm illustrated in Figure 9. Figure 21(c) presents Gauss integration points used in the integration.

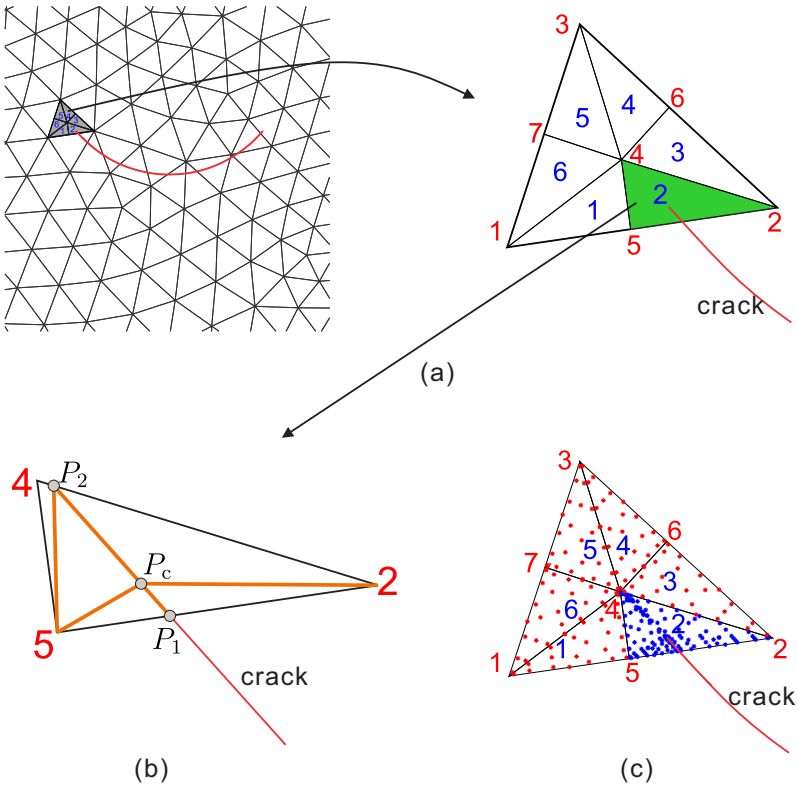

Figure 21: (a) six mini-triangles of the tip element; (b) delaunay triangulation of mini-triangle 2; (c) Gauss points in the tip element. In the figure, the initial crack is introduced as the red curve. In figure (b), point P_c is the crack tip. Point P_1 is the intersection point of the crack path and the boundary of mini-triangle 2. P_1P_c is a linear line, whose extended line touches the boundary of mini-triangle 2 at point P_2. In figure (c), blue stars correspond to Gauss points in elements with the crack tip, while red stars denote those without the crack path.

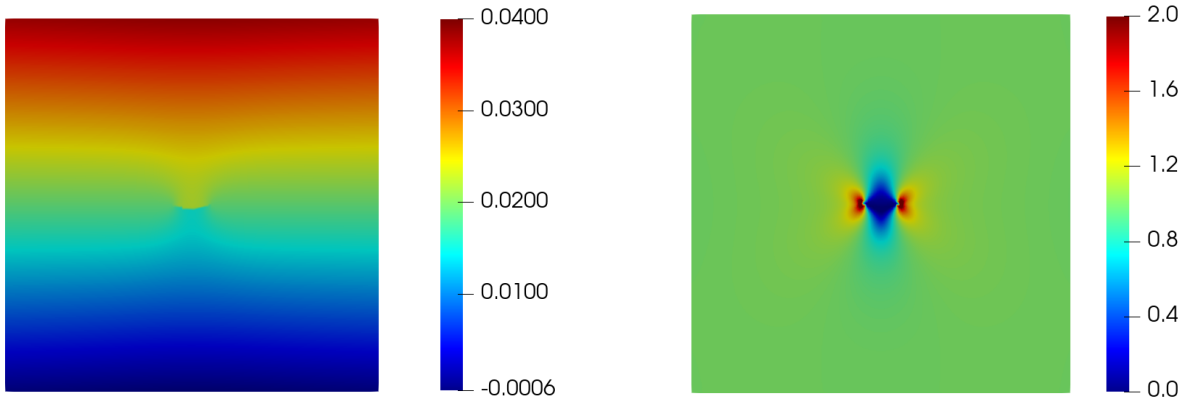

(a) contours of the displacement u_2 (b) contours of stress σ_m

Figure 22: Contour plot of the displacement u_2 and maximum principal stress σ_m.

Figure 22 illustrates the contour plot of the displacement u_2 and the maximum principal stress σ_m. In the figure, the displacement profile presents obvious jumping and sliding along the crack path due to pulling loads, see Figure 22(a). The stress is close to zero along the crack interface. The largest stress appears at the crack tip due to the stress singularity. The SIFs for different arc angles are shown in Figure 23. In the figure, the results of the proposed method are close to exact solutions. The mode-I SIFs decrease with the rise of the arc angle θ, while the mode-II SIFs increase

as θ increases.

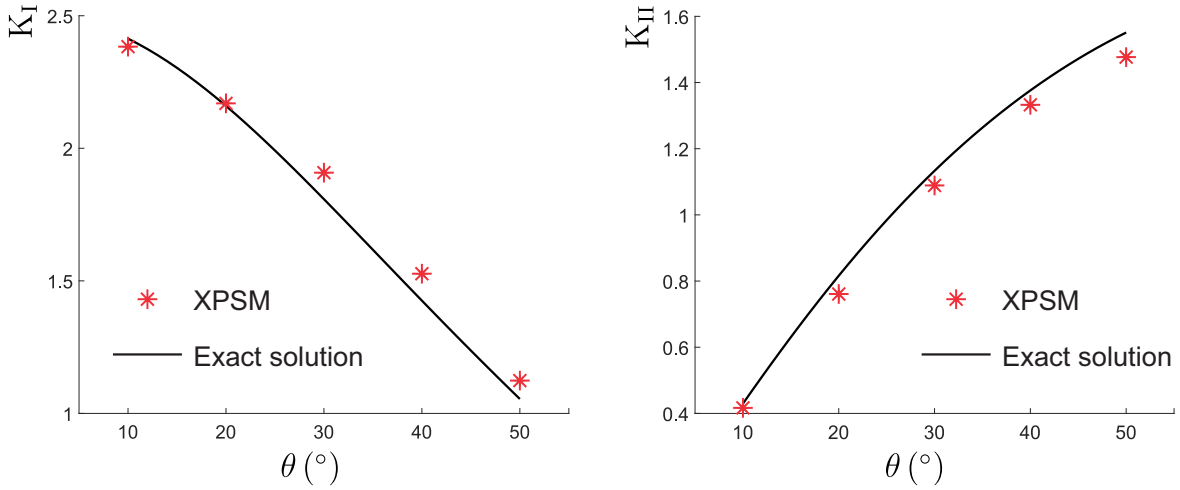

(a) mode-I SIF K_I (b) mode-II SIF K_{II}

Figure 23: SIFs with different inclination angle θ for the curved center crack problem.

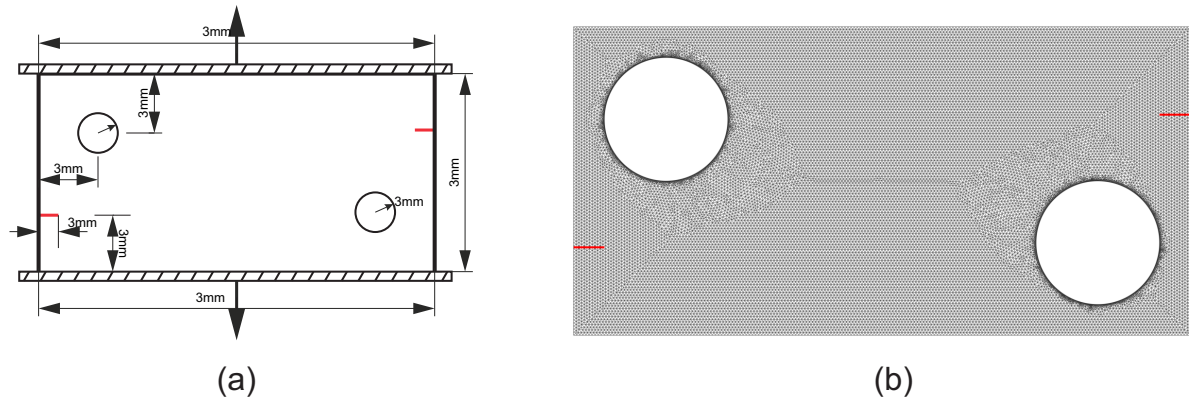

Figure 24: (a) geometry and boundary conditions for a plate with two propagating cracks; (b) initial triangulation. In figure (b), initial cracks are introduced as red lines.

4.4. A plate with two propagating cracks

In the last example, we consider a plate with two propagating cracks. This benchmark problem was introduced by Bouchard [50]. It was considered in other numerical approaches, such as polygonal FEM (PFEM) with local remeshing [49], to valid their performance. The detailed geometric parameters and boundary conditions are given in Figure 24. The bottom and top edge is forced in tension via a controlled displacement of 0.1mm, which is imposed by the Lagrange multiplier method in Section 2.3.2. The material properties of the plate are: Young's modulus $E = 98000$MPa and Poisson's ratio $\nu = 0.3$. A plain strain condition is assumed. Two initial cracks are placed at the bottom left and top right edge. A crack increment $da = 0.3$mm is chosen to enforce the crack propagation. An example of enriched control points is illustrated in Figure 25. For crack tips, two groups of tip enrichment are given in Figure 25. For Heaviside enrichment, we enrich elements touching the crack path. For the numerical integration in cracked elements, we employ the algorithm provided in Section 4.3.

In the analysis, two curved cracks will be obtained. Figure 26 depicts the propagation of two crack paths and the comparison with the solution via the numerical approach used by Khoei et al. in [49]. Obviously, due to the

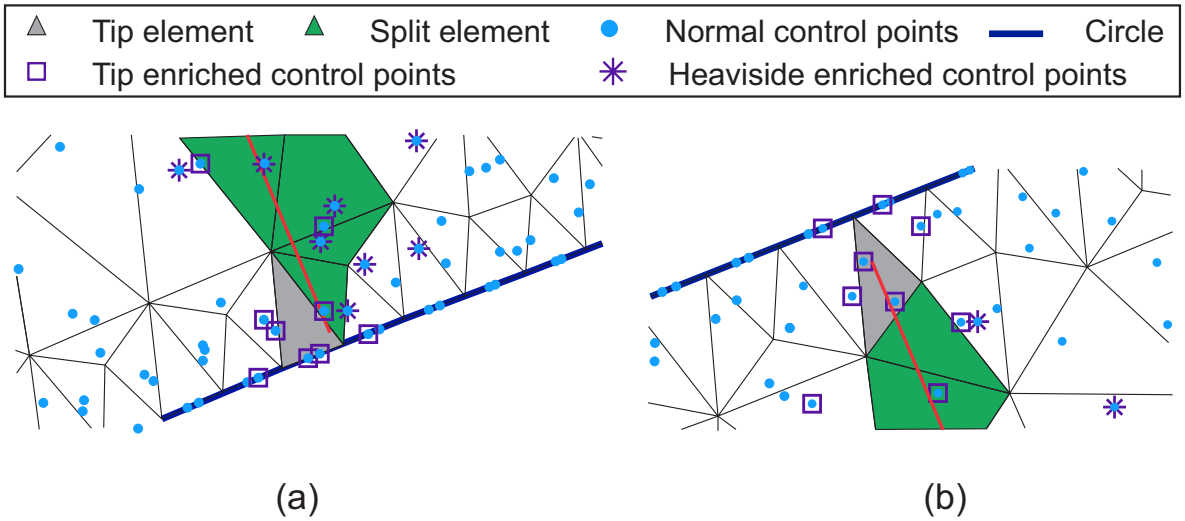

Figure 25: Various types of elements and control points for the problem. (a) left bottom cracked elements with crack tips and split elements; (b) right top cracked elements with crack tips and split elements; in the figure, cracks are introduced as red curves; the boundary of the circle is denoted as blue lines.

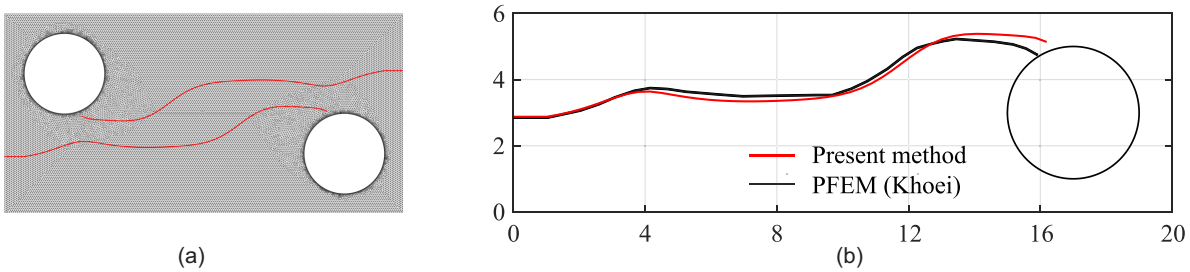

Figure 26: (a) final crack paths; (b) crack path of the left bottom crack in comparison with Khoei et al.'s simulation [49]. In figure (a), cracks are introduced as red curves.

domain symmetry, crack paths show a similar pattern. The predicted crack path compares well with that from Khoei et al.'s simulation. Figure 27 presents the displacement u_2 and the corresponding maximum principal stress σ_{m}. The displacement profile presents obvious jump between crack interfaces. The largest stress appears at the crack tip due to the stress singularity.

5. Concluding remarks

An extended Powell-Sabin scheme (XPSM) has been developed for fracture analysis. It combines Powell-Sabin finite elements with extended FEM. Powell-Sabin B-splines are employed to interpolate the displacement field and to discretize the domain. Powell-Sabin B-splines are based on triangles and are C^1 continuous with respect to the interpolation of the displacement field, also across element boundaries. This implies that the stress field is continuous, again also across element boundaries. For the analysis of crack problems Powell-Sabin B-splines have yet another important advantage, namely that the C^1 continuity in the displacement field is preserved at crack tips, unlike other discrete crack models, where the higher-order continuity breaks down at the crack tip. Due to the localized property of Powell-Sabin B-splines, basis functions are confined in cracked elements, similar to traditional XFEM. However, the higher order continuity property still holds between elements. Numerical examples show that the ability of the XPSM is very suitable for the analysis of crack problems. The C^1-continuity of Powell-Sabin B-splines improves the accuracy of the stress. In addition, comparing to the XFEM, no extra effort is needed to smooth the stress field.

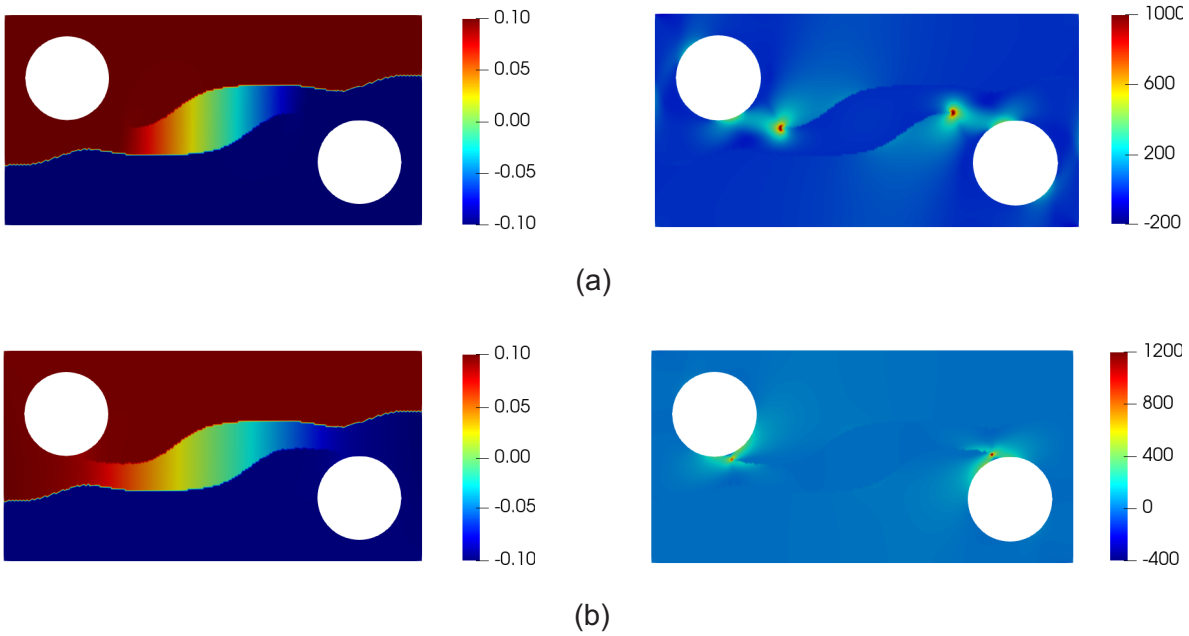

Figure 27: Contour plot of the displacement u_2 (left) and maximum principal stress σ_{m} (right) at time: (a) step 38, (b) step 45.

Acknowledgement

Financial support from the Engineering and Physical Sciences Research Council (EPSRC: EP/T033940/1) is gratefully acknowledged.

Appendix A. Crack tip displacement fields

For completeness, we present the formulations of asymptotic displacement fields under pure mode-I loadings around a straight crack tip. We impose these displacement fields as boundary conditions to approximate singular stress fields (parameterised by the stress intensity factor $\mathrm{K_I}$) around the crack tip. The asymptotic displacement fields are given as

$$\begin{aligned} u_x &= \frac{\mathrm{K_I}}{2\mu}\sqrt{\frac{r}{2\pi}}\cos\frac{\theta}{2}(\kappa-\cos\theta) \\ u_y &= \frac{\mathrm{K_I}}{2\mu}\sqrt{\frac{r}{2\pi}}\sin\frac{\theta}{2}(\kappa-\cos\theta) \end{aligned} \qquad \text{(Appendix A.1)}$$

where $\mu = E/2(1+\nu)$, $\kappa = 3-4\nu$ for plane strain and $\kappa = (3-\nu)/(1+\nu)$ for plane stress, and (r,θ) are polar coordinates with origin positioned at the crack tip. The derivatives of displacement fields with respect to Cartesian coordinates (x,y) at the crack tip read:

$$\begin{aligned} \frac{\partial u_x}{\partial x} &= \frac{\mathrm{K_I}}{4\mu\sqrt{2\pi r}}\cos\frac{\theta}{2}(-\cos\theta+\cos 2\theta+\kappa-1) \\ \frac{\partial u_x}{\partial y} &= \frac{\mathrm{K_I}}{4\mu\sqrt{2\pi r}}\sin\frac{\theta}{2}(\cos\theta+\cos 2\theta+\kappa+1) \\ \frac{\partial u_y}{\partial x} &= \frac{\mathrm{K_I}}{4\mu\sqrt{2\pi r}}\sin\frac{\theta}{2}(\cos\theta+\cos 2\theta-\kappa-1) \\ \frac{\partial u_y}{\partial y} &= \frac{\mathrm{K_I}}{4\mu\sqrt{2\pi r}}\cos\frac{\theta}{2}(\cos\theta-\cos 2\theta+\kappa-1) \end{aligned} \qquad \text{(Appendix A.2)}$$

References

[1] D. Ngo, A. C. Scordelis, Finite element analysis of reinforced concrete beams, Journal of the American Concrete Institute 64 (1967) 152–163.

[2] Y. R. Rashid, Analysis of reinforced concrete pressure vessels, Nuclear Engineering and Design 7 (1968) 334–344.

[3] J. Li, Z. S. Khodaei, M. Aliabadi, Dynamic dual boundary element analyses for cracked mindlin plates, International journal of solids and structures 152 (2018) 248–260.

[4] J. Li, Z. S. Khodaei, M. Aliabadi, Boundary element analysis of lamb wave scattering by a through-thickness crack in a plate, in: AIP Conference Proceedings, Vol. 2309, AIP Publishing LLC, 2020, p. 020007.

[5] T. Rabczuk, T. Belytschko, Cracking particles: a simplified meshfree method for arbitrary evolving cracks, International journal for numerical methods in engineering 61 (13) (2004) 2316–2343.

[6] L. Ramalho, J. Dionísio, I. Sánchez-Arce, R. Campilho, J. Belinha, Analysis of stress singularity in adhesive joints using meshless methods, Engineering Analysis with Boundary Elements 137 (2022) 29–40.

[7] T. Belytschko, Y. Y. Lu, L. Gu, Element-free galerkin methods, International journal for numerical methods in engineering 37 (2) (1994) 229–256.

[8] A. Kumar, R. Ghosh, Particularly optimized enriched element-free galerkin method (poe-efgm) for orthotropic fracture analysis of cortical bone, Engineering Fracture Mechanics 254 (2021) 107943.

[9] N. Moës, J. Dolbow, T. Belytschko, A finite element method for crack growth without remeshing, International journal for numerical methods in engineering 46 (1) (1999) 131–150.

[10] A. Latifaghili, M. Bybordiani, R. E. Erkmen, D. Dias-da Costa, An extended finite element method with polygonal enrichment shape functions for crack propagation and stiff interface problems, International Journal for Numerical Methods in Engineering 123 (6) (2022) 1432–1455.

[11] C. Song, E. T. Ooi, S. Natarajan, A review of the scaled boundary finite element method for two-dimensional linear elastic fracture mechanics, Engineering Fracture Mechanics 187 (2018) 45–73.

[12] T. Bennett, A. Rodríguez-Ferran, H. Askes, Damage regularisation with inertia gradients, European Journal of Mechanics-A/Solids 31 (1) (2012) 131–138.

[13] I. C. Mihai, A. D. Jefferson, P. Lyons, A plastic-damage constitutive model for the finite element analysis of fibre reinforced concrete, Engineering Fracture Mechanics 159 (2016) 35–62.

[14] W. Alnaas, A. Jefferson, A smooth unloading–reloading approach for the nonlinear finite element analysis of quasi-brittle materials, Engineering Fracture Mechanics 152 (2016) 105–125.

[15] L. Chen, B. Li, R. de Borst, Adaptive isogeometric analysis for phase-field modeling of anisotropic brittle fracture, International Journal for Numerical Methods in Engineering 121 (20) (2020) 4630–4648.

[16] T. Belytschko, T. Black, Elastic crack growth in finite elements with minimal remeshing, International journal for numerical methods in engineering 45 (5) (1999) 601–620.

[17] E. B. Chin, N. Sukumar, Modeling curved interfaces without element-partitioning in the extended finite element method, International Journal for Numerical Methods in Engineering 120 (5) (2019) 607–649.

[18] H. Li, J. Li, H. Yuan, A review of the extended finite element method on macrocrack and microcrack growth simulations, Theoretical and Applied Fracture Mechanics 97 (2018) 236–249.

[19] P. Samantray, R. H. Peerlings, E. Bosco, M. G. Geers, T. J. Massart, O. Rokoš, Level set-based extended finite element modeling of the response of fibrous networks under hygroscopic swelling, Journal of Applied Mechanics 87 (10) (2020).

[20] E. Mohtarami, A. Baghbanan, H. Hashemolhosseini, S. P. Bordas, Fracture mechanism simulation of inhomogeneous anisotropic rocks by extended finite element method, Theoretical and Applied Fracture Mechanics 104 (2019) 102359.

[21] S. Zonca, C. Vergara, L. Formaggia, An unfitted formulation for the interaction of an incompressible fluid with a thick structure via an xfem/dg approach, SIAM Journal on Scientific Computing 40 (1) (2018) B59–B84.

[22] A. Khoei, S. Mortazavi, Thermo-hydro-mechanical modeling of fracturing porous media with two-phase fluid flow using x-fem technique, International Journal for Numerical and Analytical Methods in Geomechanics 44 (18) (2020) 2430–2472.

[23] S. M. S. Mortazavi, P. Pirmoradi, A. R. Khoei, Numerical simulation of cold and hot water injection into naturally fractured porous media using the extended–fem and an equivalent continuum model, International Journal for Numerical and Analytical Methods in Geomechanics 46 (3) (2022) 617–655.

[24] M. Surendran, S. Natarajan, G. Palani, S. P. Bordas, Linear smoothed extended finite element method for fatigue crack growth simulations, Engineering Fracture Mechanics 206 (2019) 551–564.

[25] J. Dolbow, N. Moës, T. Belytschko, Discontinuous enrichment in finite elements with a partition of unity method, Finite elements in analysis and design 36 (3-4) (2000) 235–260.

[26] R. Rosa, H. Coda, R. Sanches, Blended isogeometric-finite element analysis for large displacements linear elastic fracture mechanics, Computer Methods in Applied Mechanics and Engineering 392 (2022) 114622.

[27] D. J. Benson, Y. Bazilevs, E. De Luycker, M.-C. Hsu, M. Scott, T. Hughes, T. Belytschko, A generalized finite element formulation for arbitrary basis functions: from isogeometric analysis to xfem, International Journal for Numerical Methods in Engineering 83 (6) (2010) 765–785.

[28] S. S. Ghorashi, N. Valizadeh, S. Mohammadi, Extended isogeometric analysis for simulation of stationary and propagating cracks, International Journal for Numerical Methods in Engineering 89 (9) (2012) 1069–1101.

[29] W. Hou, K. Jiang, X. Zhu, Y. Shen, P. Hu, Extended isogeometric analysis using b++ splines for strong discontinuous problems, Computer Methods in Applied Mechanics and Engineering 381 (2021) 113779.

[30] E. De Luycker, D. J. Benson, T. Belytschko, Y. Bazilevs, M. C. Hsu, X-fem in isogeometric analysis for linear fracture mechanics, International Journal for Numerical Methods in Engineering 87 (6) (2011) 541–565.

[31] S. BaniHani, F. M. AL-Oqla, M. Hayajneh, S. Mutawe, T. Almomani, A new approach for dynamic crack propagation modeling based on meshless galerkin method and visibility based criterion., Applied Mathematical Modelling (2022).

[32] T. Rabczuk, J.-H. Song, X. Zhuang, C. Anitescu, Extended finite element and meshfree methods, Academic Press, 2019.

[33] M. J. Powell, M. A. Sabin, Piecewise quadratic approximations on triangles, ACM Transactions on Mathematical Software (TOMS) 3 (1977) 316–325.
[34] J. O'Rourke, A. Aggarwal, S. Maddila, M. Baldwin, An optimal algorithm for finding minimal enclosing triangles, Journal of Algorithms 7 (1986) 258–269.
[35] G. Giorgiani, H. Guillard, B. Nkonga, E. Serre, A stabilized powell–sabin finite-element method for the 2d euler equations in supersonic regime, Computer Methods in Applied Mechanics and Engineering 340 (2018) 216–235.
[36] H. Speleers, C. Manni, Optimizing domain parameterization in isogeometric analysis based on powell–sabin splines, Journal of Computational and Applied Mathematics 289 (2015) 68–86.
[37] L. Chen, R. de Borst, Cohesive fracture analysis using Powell-Sabin B-splines, International Journal for Numerical and Analytical Methods in Geomechanics 43 (2019) 625–640.
[38] Y. Wang, H. Waisman, Material-dependent crack-tip enrichment functions in xfem for modeling interfacial cracks in bimaterials, International Journal for Numerical Methods in Engineering 112 (11) (2017) 1495–1518.
[39] A. R. Khoei, Extended finite element method: theory and applications, John Wiley & Sons, 2014.
[40] F. Fathi, L. Chen, R. de Borst, Extended isogeometric analysis for cohesive fracture, International Journal for Numerical Methods in Engineering 121 (20) (2020) 4584–4613.
[41] S. May, J. Vignollet, R. d. Borst, Powell–sabin b-splines and unstructured standard t-splines for the solution of the kirchhoff–love plate theory exploiting bézier extraction, International Journal for Numerical Methods in Engineering 107 (3) (2016) 205–233.
[42] H. D. Huynh, X. Zhuang, H. Nguyen-Xuan, A polytree-based adaptive scheme for modeling linear fracture mechanics using a coupled xfem–sbfem approach, Engineering Analysis with Boundary Elements 115 (2020) 72–85.
[43] L. Chen, B. Li, R. de Borst, The use of powell-sabin b-splines in a higher-order phase-field model for crack kinking, Computational Mechanics 67 (1) (2021) 127–137.
[44] S. Funken, D. Praetorius, P. Wissgott, Efficient implementation of adaptive P1-FEM in Matlab, Computational Methods in Applied Mathematics 11 (2011) 460–490.
[45] C. Geuzaine, J.-F. Remacle, Gmsh: A 3-D finite element mesh generator with built-in pre-and post-processing facilities, International Journal for Numerical Methods in Engineering 79 (2009) 1309–1331.
[46] J. Gu, T. Yu, S. Tanaka, H. Yuan, T. Q. Bui, et al., Crack growth adaptive xiga simulation in isotropic and orthotropic materials, Computer Methods in Applied Mechanics and Engineering 365 (2020) 113016.
[47] T. Yu, T. Q. Bui, Numerical simulation of 2-d weak and strong discontinuities by a novel approach based on xfem with local mesh refinement, Computers & Structures 196 (2018) 112–133.
[48] E. E. Gdoutos, Fracture mechanics: an introduction, Vol. 263, Springer Nature, 2020.
[49] A. Khoei, R. Yasbolaghi, S. Biabanaki, A polygonal finite element method for modeling crack propagation with minimum remeshing, International journal of fracture 194 (2) (2015) 123–148.
[50] P.-O. Bouchard, F. Bay, Y. Chastel, Numerical modelling of crack propagation: automatic remeshing and comparison of different criteria, Computer methods in applied mechanics and engineering 192 (35-36) (2003) 3887–3908.